




Prediction of phase transition and time-varying dynamics of the $(2 + 1)$ -dimensional Boussinesq equation by parameter-integrated physics-informed neural networks with phase domain decomposition

Haiyi Liu ¹, Lei Wang ^{1,*}, Yabin Zhang ², Gui Lu,³ and Lei Liu⁴

¹*School of Mathematics and Physics, North China Electric Power University, Beijing 102206, People's Republic of China*

²*School of Control and Computer Engineering, North China Electric Power University, Beijing 102206, People's Republic of China*

³*School of Energy Power and Mechanical Engineering, North China Electric Power University, Beijing 102206, People's Republic of China*

⁴*College of Mathematics and Statistics, Chongqing University, Chongqing 401331, People's Republic of China*



(Received 27 January 2023; accepted 13 September 2023; published 6 October 2023)

A meaningful topic that needs to be explored in the field of nonlinear waves is whether a neural network can reveal the phase transition of different types of waves and novel dynamical properties. In this paper, a physics-informed neural network (PINN) with parameters is used to explore the phase transition and time-varying dynamics of nonlinear waves of the $(2 + 1)$ -dimensional Boussinesq equation describing the propagation of gravity waves on the surface of water. We embed the physical parameters into the neural network for this purpose. Via such algorithm, we find the exact boundary of the phase transition that distinguishes the periodic lump chain and transformed wave, and the inexact boundaries of the phase transition for various transformed waves are detected through PINNs with phase domain decomposition. In particular, based only on the simple soliton solution, we discover types of nonlinear waves as well as their interesting time-varying properties for the $(2 + 1)$ -dimensional Boussinesq equation. We further investigate the stability by adding noise to the initial data. Finally, we perform the parameters discovery of the equation in the case of data with and without noise, respectively. Our paper introduces deep learning into the study of the phase transition of nonlinear waves and paves the way for intelligent explorations of the unknown properties of waves by means of the PINN technique with a simple solution and small data set.

DOI: [10.1103/PhysRevE.108.045303](https://doi.org/10.1103/PhysRevE.108.045303)

I. INTRODUCTION

The investigation of nonlinear waves is a significant topic in soliton theory [1]. These wave phenomena exist in nature, experimental observations, and engineering applications widely. The field is broad and encompasses such areas as fluids [2], Bose-Einstein condensation [3–5], plasmas [6,7], nonlinear optics [8,9], superfluid [10,11], and magnetics [12]. A variety of nonlinear waves to date have been discovered, for example, solitons, breathers, and rogue waves, to name a few. A soliton is a localized wave produced by a balance between dispersion and nonlinearity, and their interactions are usually characterized by elastic collisions [13]. A breather on a constant background is an oscillating localized structure, appearing not only in conservative systems but also in dissipative ones [14–16]. The breather family mainly consists of two members, namely, the Akhmediev breathers [14,15] and Kuznetsov-Ma breathers [16]. An Akhmediev breather is periodic in the transverse direction [14,15], while a Kuznetsov-Ma breather is periodic in the propagation direction [16]. If the period in either time or space approaches infinity, then the limit case of each wave is a Peregrine soliton [17–19]. Such wave is localized both in time and in space and thus describes a rogue wave [20] (which “appears from nowhere and

disappears without a trace” [21]). These nonlinear waves were first studied in low-dimensional models, such as the Korteweg–de Vries equation [22], nonlinear Schrödinger equation [23], and Boussinesq equations [24]. As the dimension increases the waves may show new properties different from low-dimensional cases. For instance, the rogue waves in the Davey-Stewartson equation appear in the form of line rogue waves which “arise from the constant background with a line profile and then disappear into the constant background again” [25]. As the limiting case of the periodic lump chain, the single lump solution is another type of high-dimensional rational one and localized in space in all directions [26–32]. It is generally not a short-lived structure, unlike the Peregrine soliton. These findings show that high-dimensional models, indeed, exhibit some interesting nonlinear phenomena that do not exist in low-dimensional ones.

In addition to the above waves, other types of nonlinear waves converted from these basic ones were also reported [33–40]. In particular, the phase transition of waves has attracted considerable interest in recent years [33–40]. In such context, a breather can be seen as a nonlinear superposition of two different types of wave components. One is the solitary wave component and the other is the periodic wave one, the characteristic directions of which are usually different. When both components have the same direction, then types of transformed waves can be observed, including the bell-shaped soliton, multipeak soliton, periodic wave, and

*Corresponding author: 50901924@ncepu.edu.cn

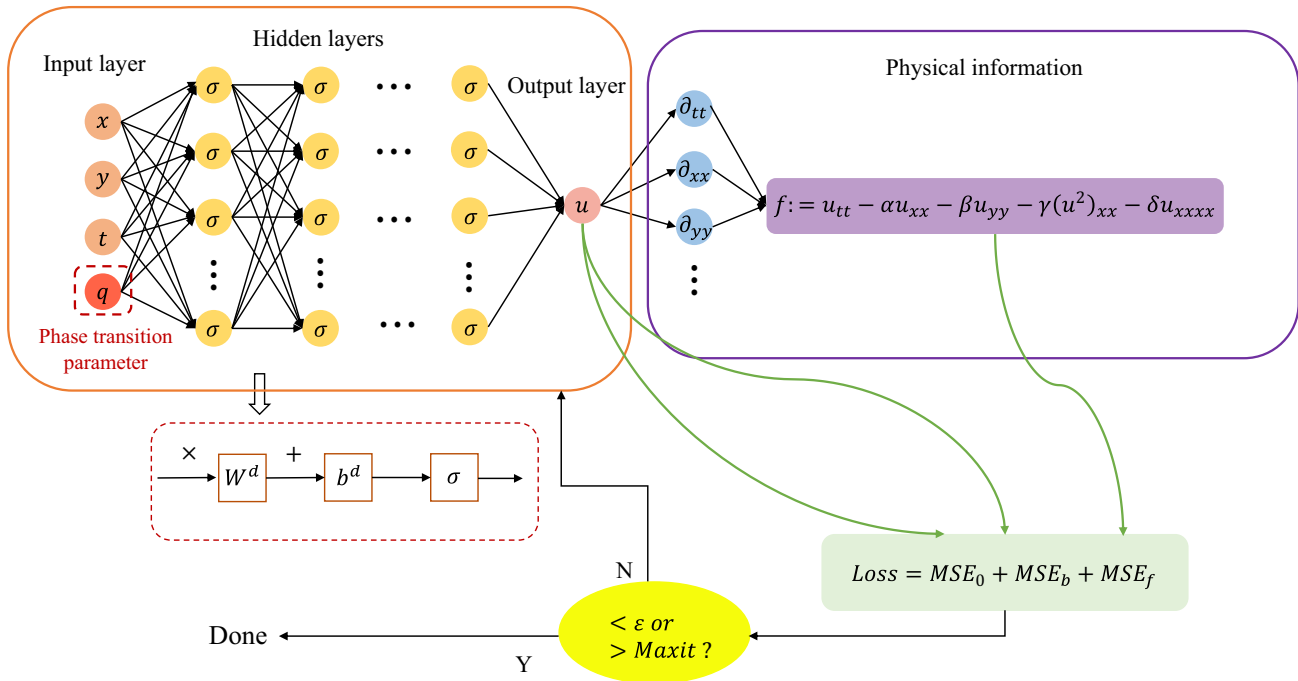


FIG. 1. The structure of the PINN with a single parameter for the (2 + 1)-dimensional Boussinesq equation. It is divided into two parts, namely, the neural network and physical information. The neural network part includes the input layer, hidden layers, and output layer. The mapping relationship is shown in the dashed red box. In the part of physical information, the residual of the equation is added to the loss function as a physical constraint, which constitutes the loss function together with the loss of initial and boundary conditions. The parameter (q) is embedded in the input layer, which provides the neural network with the ability of exploring the phase transition between the periodic lump chain and transformed wave.

rational W-shaped soliton [33–39]. In the low-dimensional case, the transformed waves appear as a result of higher-order effects [33–38]. Such systems include the Hirota equation [35], Lakshmanan-Porsezian-Daniel equation [37], Sasa-Satsuma equation [41], nonautonomous Hirota equation [38], and so on. Note that there is no an analog in the standard nonlinear Schrödinger equation. In addition, transformed waves also exist in such coupled systems as the coupled Hirota system [36], nonlinear Schrödinger-Maxwell-Bloch system [42], and multicomponent AB systems [43–45]. As mentioned above, types of nonlinear waves show different physical properties in the high-dimensional case. The same situation holds for transformed waves. In the (2 + 1)-dimensional Ito equation, the multipeak soliton exhibits an obvious shape-changed characteristic during its propagation, also known as time-varying dynamics [46]. This is mainly due to the fact that different kinds of wave components have different velocities, which leads to the dynamic change of the superposition region with time.

The neural network is one of the main application models of deep learning, which has achieved great success in many fields, such as speech recognition [47], image recognition [48], and cognitive science [49]. In recent years, the deep neural network (DNN) has been applied to solve important practical problems due to its excellent ability [50]. However, when faced with complex problems, a large amount of data is difficult to obtain and this method lacks prior information of the corresponding problems such as physical law and professional knowledge. In view of the above issues, the

physics-informed neural network (PINN), which is a neural network with physical laws, is used to explore the forward and inverse problems of some fundamental partial differential equations (PDEs) [51]. Such technique is also extended to solve fractional differential equations [52], integrodifferential equations [53], and stochastic differential equations [54]. Notably, domain decomposition approaches based on the PINN framework have been developed in order to solve certain complex PDEs [55,56]. In addition, the PINN method is devoted to investigate integrable (1 + 1)-dimensional PDEs [57–62]. Recently, Ref. [63] revealed the distortion of the Peregrine soliton when a Gaussian-type perturbation is added to the initial condition. We note that the PINN algorithm is rarely used to study the mechanism of the phase transition of nonlinear waves and to predict unknown dynamics. In particular, there are few investigations on time-varying dynamics via such technique.

In this paper, we consider the (2 + 1)-dimensional Boussinesq equation. In shallow water, it is well known that the Korteweg–de Vries equation is a model of a unidirectional moving wave [22]. Instead, in the context of a deep water wave, the counterpart is known as the nonlinear Schrödinger equation [23]. Further, if oblique interactions or slightly curved wave fronts exist, then the governing equation becomes the Kadomtsev-Petviashvili equation [64]. Such equation serves as a model for long waves with weak nonlinear restoring force and frequency dispersion [26,65]. Unlike the above models, the Boussinesq equation describes the propagation of long waves in shallow water in opposite

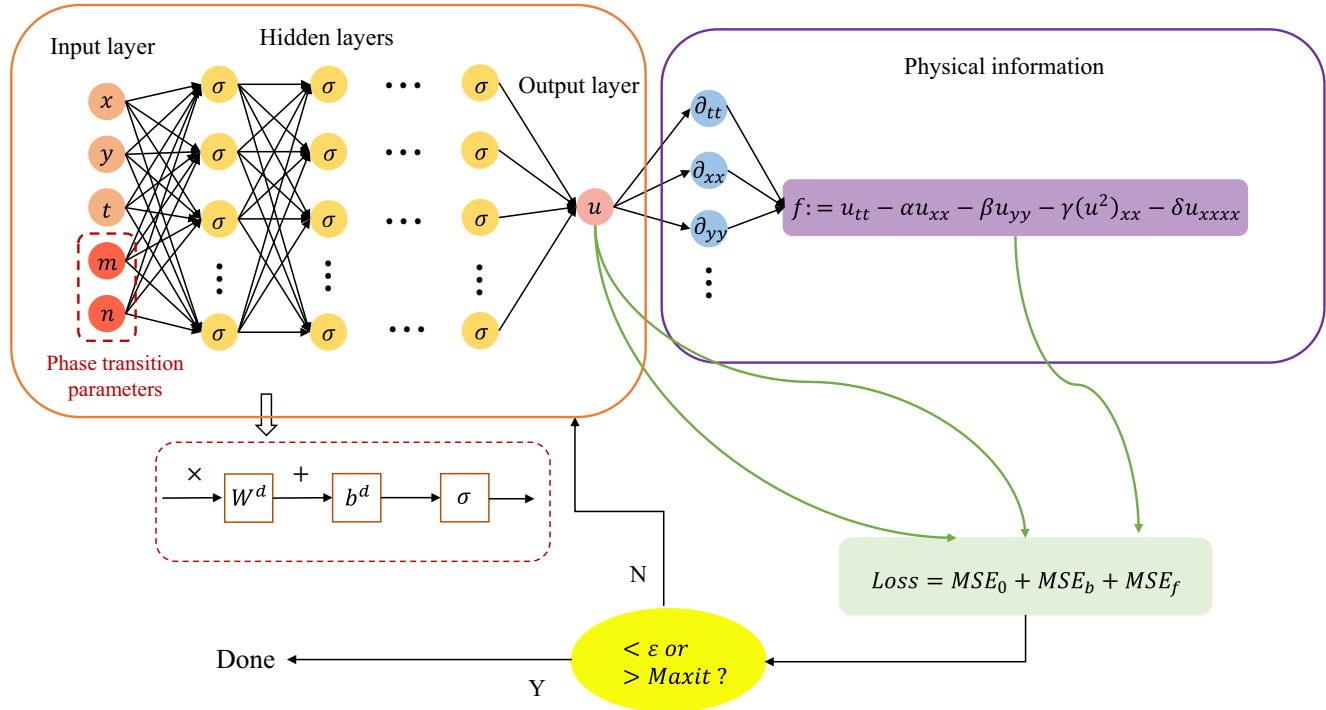


FIG. 2. The structure of the PINN with two parameters. The overall structure is the same as in Fig. 1. Unlike Fig. 1, the parameter q is replaced by m and n that are responsible for classifying different types of transformed waves.

directions [24]. Similar to the Kadomtsev-Petviashvili equation, the $(2 + 1)$ -dimensional Boussinesq equation is also obtained in the two-dimensional case. It has weak dependence on the second spatial variable, and it reads as [66]

$$u_{tt} - \alpha u_{xx} - \beta u_{yy} - \gamma (u^2)_{xx} - \delta u_{xxxx} = 0, \quad (1)$$

in which $u(x, y, t)$ is a real-valued function with time variable t and space variables x and y , the subscripts are represented as partial differentials, and the parameters α, β, γ , and δ are nonzero constants. Equation (1) can be used to describe the propagation of gravity waves over water, in particular the head-on collision of oblique waves [66]. Johnson *et al.* obtained the exact and general solitary-wave, two-soliton, and

resonant solutions of Eq. (1) by the Hirota bilinear method, and also have proved that it does not belong to the class of completely integrable equations [66].

Here, we consider the PINN with physical parameters for studying Eq. (1). By such neural network, we first give the boundary of the phase transition which can distinguish between transformed and nontransformed waves. Subsequently, we predict a series of transformed waves on the parameter lines. In particular, we explore two approximate boundaries of the phase transition in the parameter phase plane through the parametrized PINN with phase domain decomposition. Further, according to data derived solely from the soliton solution [66], we show types of solutions and a dynamical property of Eq. (1), namely, the time-varying dynamics. It should be pointed out that all the data used in this paper are obtained by auxiliary processing of the soliton solution in Ref. [66]. This shows that the PINN technique can discover solutions and physical mechanisms with only a simple known solution and a small amount of simple data.

II. METHOD

In this section, we first review the DNN and PINN methods. Then we put forward the PINN algorithm with physical parameters and phase domain decomposition for studying the transition mechanism of Eq. (1).

In general, the feed-forward neural network can complete complex mapping from input space to output space through the actions of multiple nonlinear functions [67]. If the feed-forward neural network has D layers, it includes an input layer, $D - 1$ hidden layers, and an output layer, and each layer is assumed to have n_d neurons ($d = 0, 1, \dots, D$). The neural

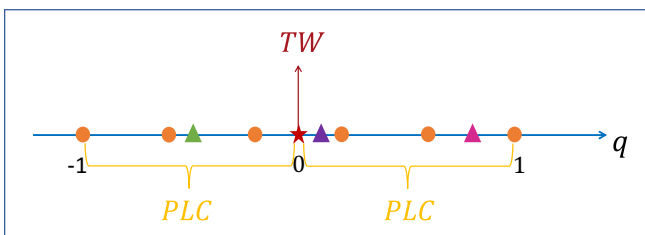


FIG. 3. Phase transition prediction. The orange dots describe the training data required by the neural network. The star and triangles stand for the predicted points. The transformed wave is denoted as TW, and the periodic lump chain is expressed as PLC. By the PINN method with a single phase transition parameter, it can be found that the position of the red star is responsible for the phase transition boundary, that is, the state transition will appear under this condition. The value of the parameter q represents the wave number of the direction y in the $(2 + 1)$ -dimensional Boussinesq equation.

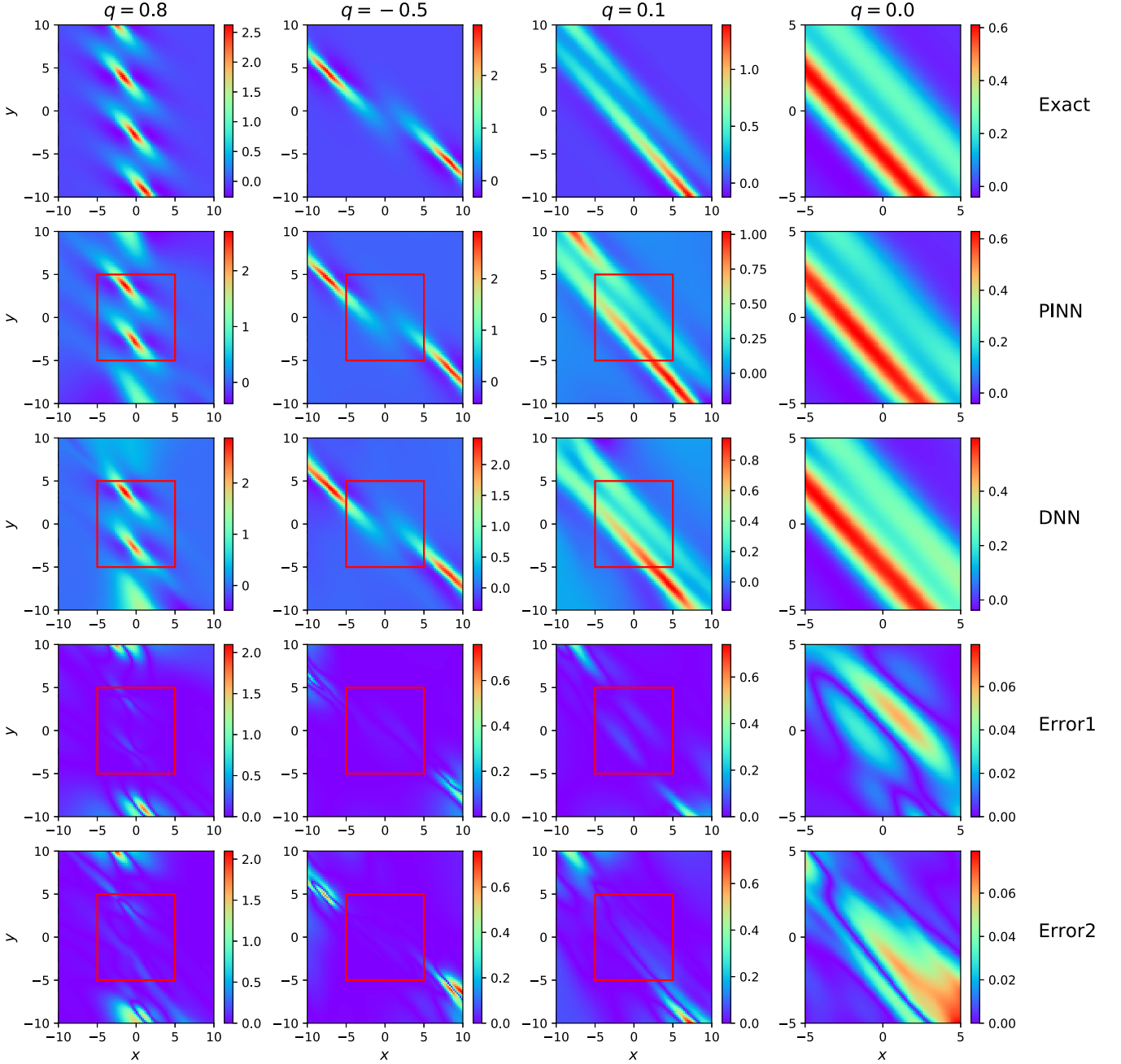


FIG. 4. Prediction of the waves under different values of the parameter q via the PINN and DNN methods at time $t = 0$. The value of q in each column corresponds to the triangles and star in Fig. 3, respectively. The plots in the first three rows describe the results from the analytical, PINN, and DNN methods, respectively. In the last two rows, Error 1 is the absolute errors between the PINN and exact results, and Error 2 is the absolute errors between the DNN and exact results. The areas outside the red boxes represent the results and errors of the extrapolation, respectively. From the evolution of the four plots in the second row, the PINN method can explore the phase transition point effectively, i.e., $q = 0$. The parameters are $\alpha = -1$, $\beta = -1$, $\gamma = 3$, and $\delta = 1$.

network can be expressed as follows:

$$\Phi^{d+1}(\mathbf{x}^d) = \mathbf{W}^{d+1}\mathbf{x}^d + \mathbf{b}^{d+1}, \quad d = 0, 1, \dots, D-1,$$

$$u(\mathbf{x}^0; \theta) = (\Phi^D \circ \sigma \circ \Phi^{D-1} \circ \dots \circ \sigma \circ \Phi^1)(\mathbf{x}^0), \quad (2)$$

where Φ is the affine transformation, \circ is the composition operator, σ is the activation function, $\theta = \{\mathbf{W}^d, \mathbf{b}^d\}_{d=1}^D$ represents the set of all trainable parameters, and \mathbf{W}^d and \mathbf{b}^d stand

for the weights matrix and biases from the $(d-1)$ th layer to the d th layer. The output value of the d th layer is expressed as \mathbf{x}^d . It is worth noting that the input value of each layer is the output value of the previous layer. $u(\mathbf{x}^0; \theta)$ is the predicted solution, which is the output of the last layer of the neural network.

For the DNN method, the loss function, namely, the mean square error (MSE) of the predicted and exact solutions, is

TABLE I. Comparison of the relative L_2 errors of the PINN and DNN methods under different values of the parameter q at time $t = 0$.

Methods	The relative L_2 error			
	$q = 0.8$	$q = -0.5$	$q = 0.1$	$q = 0$
PINN	2.321429×10^{-1}	4.240088×10^{-2}	7.849895×10^{-2}	7.235301×10^{-2}
DNN	1.261558×10^{-1}	3.323374×10^{-2}	1.013984×10^{-1}	1.005916×10^{-1}

defined in the following form:

$$\text{Loss} = \frac{1}{N_u} \sum_{i=1}^{N_u} |u^i(\mathbf{x}^0; \theta) - u_E^i|^2, \quad (3)$$

where N_u is the number of the training data points, $u(\mathbf{x}^0; \theta)$ is the predicted solution, and u_E is the exact solution. By optimizing the parameters in the neural network, the value of the loss function can be minimized.

Next, we aim to review the PINN algorithm [51]. We define the residual of Eq. (1) as

$$f := u_{tt} - \alpha u_{xx} - \beta u_{yy} - \gamma (u^2)_{xx} - \delta u_{xxxx}, \quad (4)$$

where u is the real-valued solution. The residual f can be regarded as a physical constraint to be added to the neural network. The corresponding partial derivatives are obtained by the automatic differentiation [68]. The loss function is defined as

$$\text{Loss} = \text{MSE}_0 + \text{MSE}_b + \text{MSE}_f, \quad (5)$$

where

$$\begin{aligned} \text{MSE}_0 &= \frac{1}{N_0} \sum_{i=1}^{N_0} |u_0^i(\mathbf{x}_0^0; \theta) - u_{E0}^i|^2, \\ \text{MSE}_b &= \frac{1}{N_b} \sum_{i=1}^{N_b} |u_b^i(\mathbf{x}_b^0; \theta) - u_{Eb}^i|^2, \\ \text{MSE}_f &= \frac{1}{N_f} \sum_{i=1}^{N_f} |f(x_f^i, y_f^i, t_f^i)|^2. \end{aligned} \quad (6)$$

N_0 , N_b , and N_f stand for the number of samples selected from the initial, boundary, and internal data, respectively. $u_0(\mathbf{x}_0^0; \theta)$ and u_{E0} represent the predicted and exact solutions of the sample points that satisfy the initial condition. $u_b(\mathbf{x}_b^0; \theta)$ and u_{Eb} are responsible for the predicted and exact solutions on the boundary. The loss function consists of the errors on the initial, boundary, and internal data, i.e., MSE_0 , MSE_b , and MSE_f .

In order to study the phase transition of nonlinear waves, we embed a physical parameter q into the neural network, which can distinguish between the periodic lump chain and transformed waves. The introduction of physical parameters into neural networks can increase the generalization ability in terms of the corresponding mechanisms, especially for the

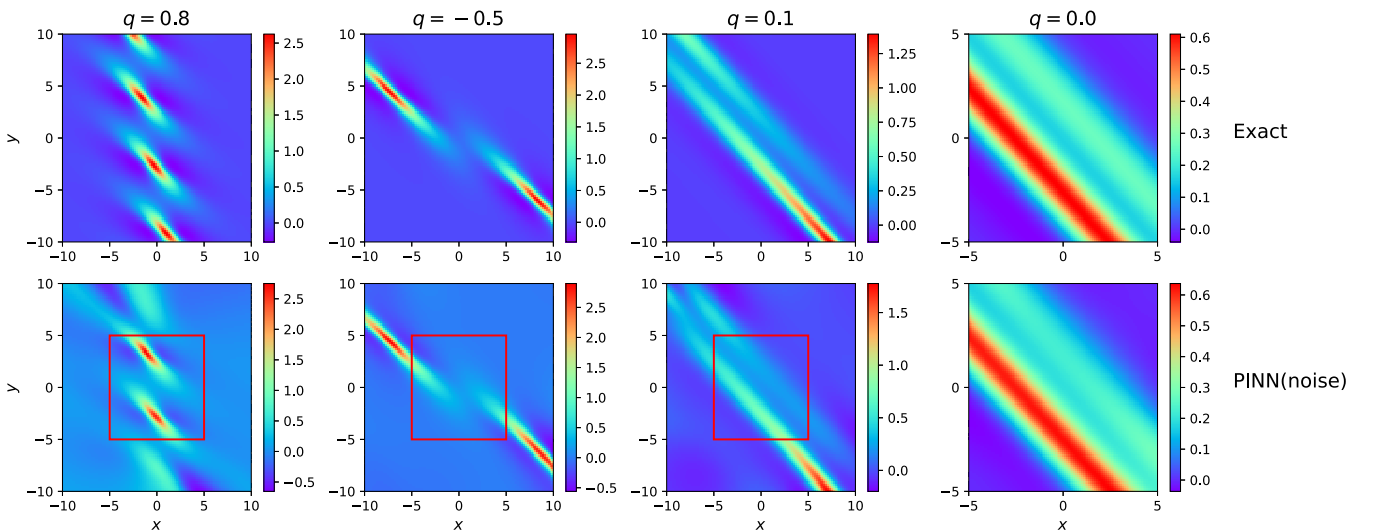


FIG. 5. Prediction of the waves under different values of the parameter q with the initial data doped with 10% noise. The value of the parameter q in each column corresponds to the triangles and star in Fig. 3, respectively. The plots describe the exact and the predicted results of the PINN method, respectively. The areas outside the red boxes are the results of the extrapolation. Although the initial data are doped with noise, the PINN method can still explore effectively the position of the phase transition, i.e., $q = 0$. The parameters are $\alpha = -1$, $\beta = -1$, $\gamma = 3$, and $\delta = 1$.

TABLE II. The relative L_2 errors of the PINN method under different values of the parameter q . The initial data are doped with 10% noise.

Method	The relative L_2 error			
	$q = 0.8$	$q = -0.5$	$q = 0.1$	$q = 0$
PINN	2.245922×10^{-1}	2.786054×10^{-2}	1.023077×10^{-1}	9.893663×10^{-2}

ability to predict new wave phenomena. Figure 1 shows the structure diagram of the PINN with the parameter q for Eq. (1) clearly. The predicted solution can be described by a nonlinear function that depends on the temporal and spatial variables and the parameter q . This means that PINN can not only predict the evolution information of the solution in the temporal and spatial domain, but also detect the variation of the parameter domain. When the neural network is trained successfully, we enter each value of the parameter q , and the profile of the corresponding wave can be observed. By utilizing such technique, we can detect the type and shape of a nonlinear wave at any position on the parameter line. However, the above algorithm with single parameter q is insufficient to detect the phase transition for different types of transformed waves. In that regard, the other two parameters m and n , which determine the phase transition for various transformed waves, are embedded in the neural network. This is shown in the framework of Fig. 2. These two physical parameters provide the neural network the ability to distinguish the localization and oscillation of different types of transformed waves. However, there are some challenges for exploring phase transition on the whole parameter plane. We here adopt the PINN with phase domain decomposition (pPINN), that is, the phase space is decomposed into several subdomains, and each subdomain has a respective neural network with the parameters m and n . This detailed exploration will be presented in Sec. IV.

In all experiments in this paper, we choose the tanh function as the activation function, and the network structure, collocation points, and spatiotemporal domain for each experiment are listed in Table VII in Appendix A. In addition, for several experiments, to facilitate the comparison of the performance of the PINN and DNN methods, we construct the same neural network structure and the number of training points. Before training, we need to initialize the parameters of the network, using the Xavier initialization method [69] for weights and setting the initial values of the biases to zero. Accordingly, Adam [70] and L-BFGS algorithms [71] are used to optimize the parameters. In addition, we use the relative L_2 error (ϵ_1) and absolute error (ϵ_2) to evaluate the performance of the algorithms, as follows:

$$\epsilon_1 = \frac{\|u_{\text{exact}} - u_{\text{pred}}\|_2}{\|u_{\text{exact}}\|_2}, \quad (7)$$

$$\epsilon_2 = |u_{\text{pred}} - u_{\text{exact}}|, \quad (8)$$

where u_{exact} and u_{pred} are the exact and predicted solutions, respectively.

Moreover, for the following experiments, we obtain the required label data after auxiliary processing through the simple soliton solution, which is produced in Ref. [66]. The analytical

expression of the second-order solution of Eq. (1) reads as

$$u = -2 \frac{\partial^2}{\partial x^2} \log f, \quad f = 1 + e^{\theta_1} + e^{\theta_2} + A_{12} e^{\theta_1 + \theta_2}, \quad (9)$$

where

$$\theta_i = k_i x + l_i y - \omega_i t + \alpha_i, \quad i = 1, 2,$$

$$\omega_i = \varepsilon_i (k_i^2 + k_i^4 + l_i^2)^{\frac{1}{2}}, \quad \varepsilon_i = \pm 1,$$

$$A_{12} = \frac{D - 6k_1^2 k_2^2}{D},$$

$$D = k_1 k_2 + l_1 l_2 - \omega_1 \omega_2 + k_1 k_2 (2k_1^2 + 3k_1 k_2 + 2k_2^2), \quad (10)$$

and k_i, l_i , and α_i ($i = 1, 2$) are free constants. In Ref. [66], the specific values of the parameters for the solution are, respectively, taken as $\alpha = 1$, $\beta = 1$, $\gamma = -3$, and $\delta = 1$.

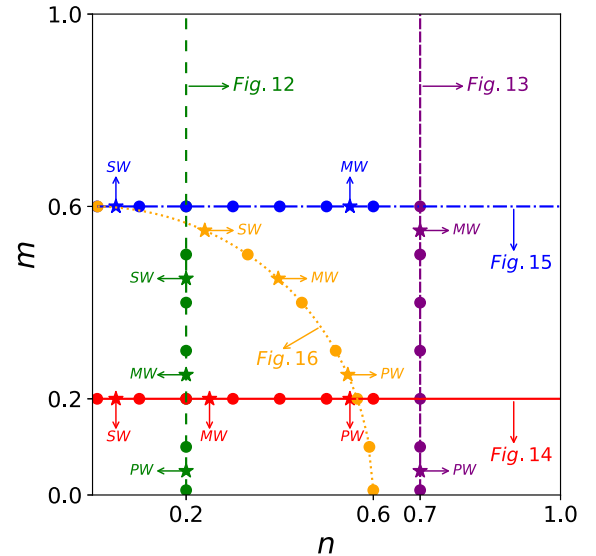


FIG. 6. Parameter plane of phase transition for transformed waves. The five different lines in the (m, n) plane represent different sets of experiments with a single parameter. The dots stand for the training data required by different neural networks. The stars are the predicted points. Through the following experiments, we can predict the structure of the wave at each star. “SW,” “MW,” and “PW” stand for the solitary wave, W- and M-shaped soliton, and periodic wave, respectively. The five lines $n = 0.2$, $n = 0.7$, $m = 0.2$, $m = 0.6$, and $m^2 + n^2 = 0.36$ are depicted by the dashed green line, densely dashed purple line, solid red line, dash-dotted blue line, and dotted orange line, respectively.

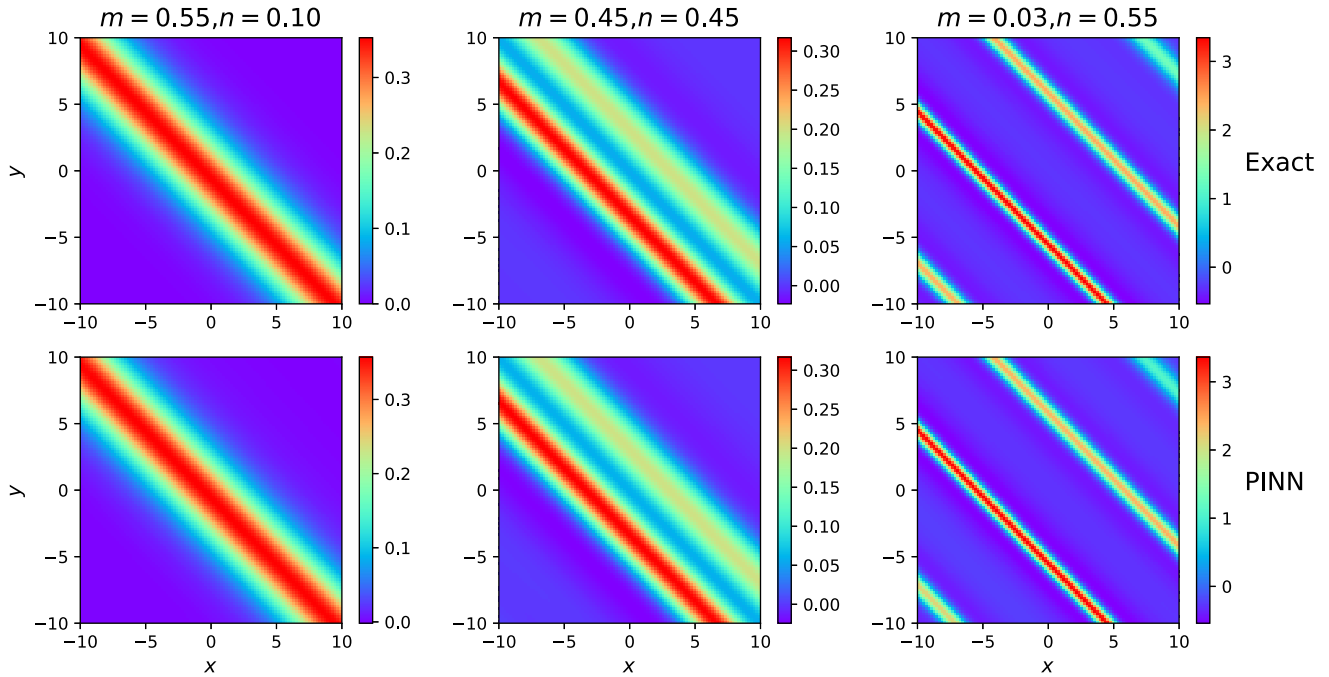


FIG. 7. Prediction of transformed waves on the whole parameter plane by means of the PINN method with two phase transition parameters. We hereby present three different results at the corresponding phase space coordinates.

III. PREDICTION OF THE PHASE TRANSITION BOUNDARY

In this section, we reveal the exact boundary of the phase transition for the periodic lump chain and transformed wave based on the above neural network. Such boundary can tell us under what conditions the waves undergo the transitions and the corresponding types of waves that can be observed. Here, we mainly use the PINN with a single phase transition parameter to achieve this. The input value of the neural network is set to $\mathbf{x}^0 = \{x, y, t, q\}$, where the value of the parameter q is the wave number of the direction y in the equation.

As indicated in Fig. 3, the periodic lump chains are formed at the orange dots, which are used as the training data of the neural network. The points of other styles are the ones that need to be predicted. The green triangle represents $q = -0.5$, the red star is the case in which the value of parameter q is equal to zero, the purple triangle marks the position where $q = 0.1$, and the pink triangle stands for $q = 0.8$. In particular, we can obtain the dynamical solution corresponding to any value of the parameter q by using the algorithm.

To observe the performance of the PINN method for exploring the transition mechanism, we show patterns of waves with different values of the parameter q at fixed time in Fig. 4. The value of the parameter q in each column corresponds to the pink triangle, green triangle, purple triangle, and red star in Fig. 3, respectively, and the dynamical solutions with these wave numbers do not serve as the training data. The plots in the first row demonstrate the structures of the exact solutions with different values of the parameter q , from a periodic lump chain to a quasisoliton to a soliton. The plots in the second and third rows show the predicted results of the PINN and DNN methods, respectively. In the last two lines, the absolute errors between the exact and predicted solutions from both

techniques are exhibited, respectively. We should point out, as shown in Fig. 4, that the prediction in the red boxes cannot

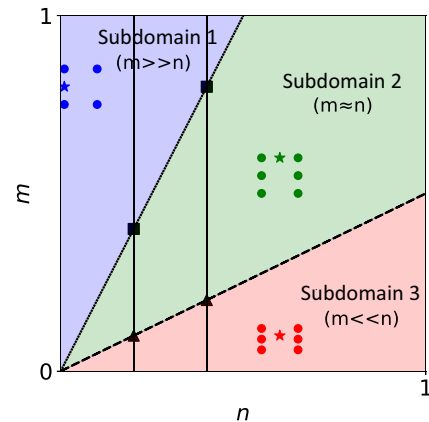


FIG. 8. Prediction of phase transition for transformed waves. The (m, n) plane is divided into three domains. The dots stand for the training data required by different neural networks in the domains. The stars represent the predicted positions. At the positions of the squares or triangles, the transformed waves exhibit roughly the same locality and oscillation, respectively. By using the pPINNs method, two approximate boundaries can be obtained in the (m, n) plane, which are responsible for distinguishing different types of transformed waves. The waves generated in subdomain 1 are the quasisolitary waves, the waves in subdomain 2 show the W- and M-shaped profiles, and the multipole solitons appear in subdomain 3. In general, it is a continuous state of the evolution for transformed waves. Therefore, whether it is based on the analytical or PINN methods, we can only give approximate phase transition boundaries. The values of the parameters m and n represent the wave numbers of the solitary wave and periodic wave components, respectively.

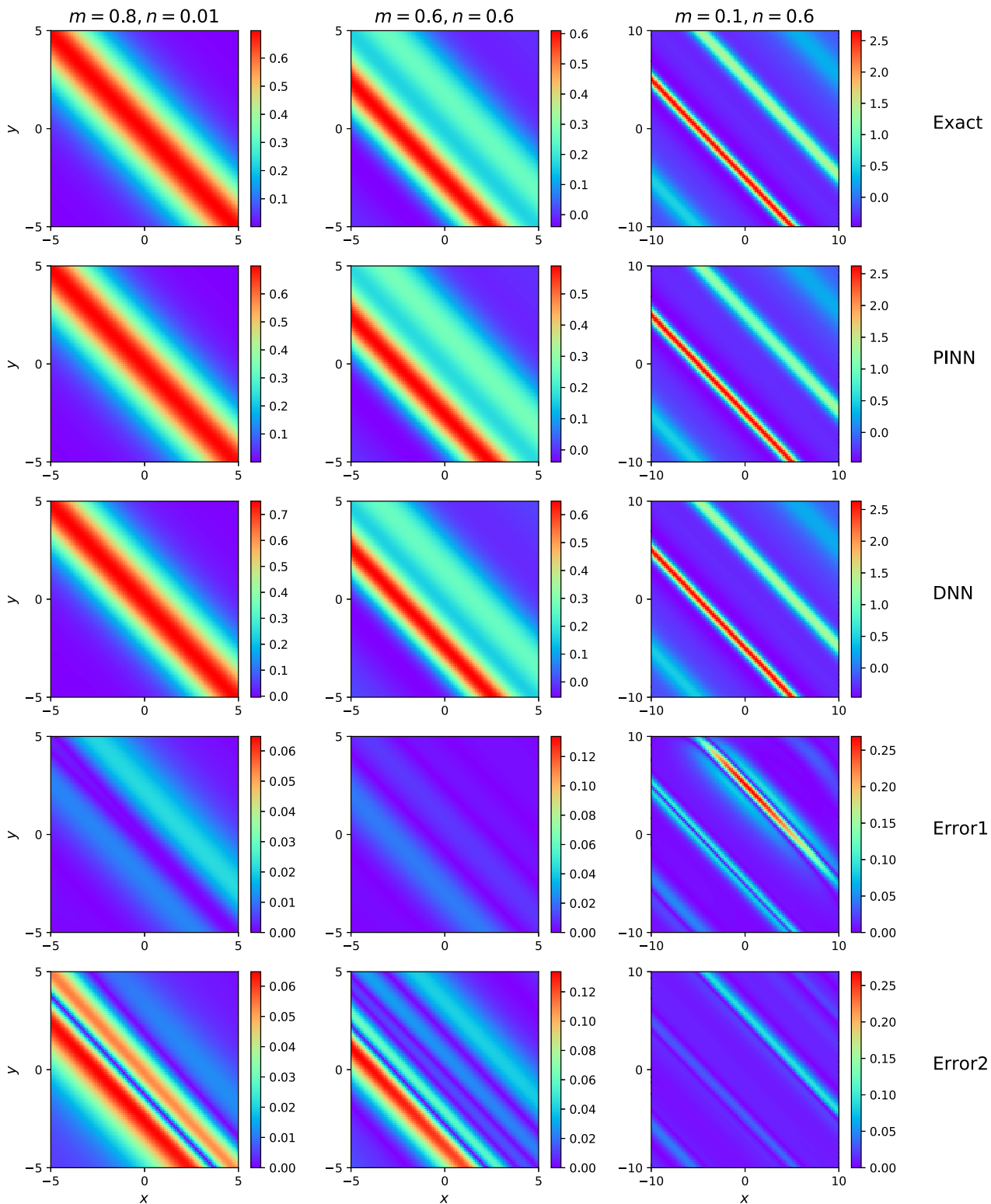


FIG. 9. Prediction of transformed waves under different sets of the parameters m and n based on the PINN and DNN methods with two parameters at time $t = 0$. The values of the parameters m and n in each column correspond to the stars in Fig. 8. The plots in the first three rows are responsible for the exact solutions, and predicted results of both methods, respectively. In the last two rows, Error 1 is the absolute errors between the exact and predicted results of the PINN method, and Error 2 is the absolute errors between the exact and predicted results of the DNN method. According to the changes of three plots in the second row, the approximate phase transition boundaries can be found. In subdomain 1, the parameters are $\alpha = -8, \beta = 1, \gamma = 3$, and $\delta = 1$. In subdomain 2 and subdomain 3, the parameters are $\alpha = -1, \beta = -1, \gamma = 3$, and $\delta = 1$.

TABLE III. Comparison of the relative L_2 errors of the PINN and DNN methods under different sets of parameters m and n at $t = 0$.

Methods	Types	The relative L_2 error		
		$m = 0.8, n = 0.01$	$m = 0.6, n = 0.6$	$m = 0.1, n = 0.6$
PINN		2.824649×10^{-2}	3.377881×10^{-2}	3.036418×10^{-2}
DNN		8.593180×10^{-2}	1.629850×10^{-1}	3.570560×10^{-2}

cover completely the pattern of such wave. Fortunately, it is not a difficult problem to fix. By extrapolating the domain, a complete periodic lump chain can be observed in the second column. Notably, the extrapolation on the domains is just to describe the complete characteristics of the wave, instead of the abilities of the algorithms. From the first and second columns in Fig. 4, one can observe that the periodic lump chains are displayed when the value of the parameter q goes from 0.8 to -0.5 . Further, we find that a quasisoliton state is shown when the value of the parameter q is equal to 0.1, while here it remains essentially the behavior of the periodic lump chain. Interestingly, if the value of the parameter q is equal to zero, the soliton state appears in the fourth column. In the second row in Fig. 4, we discover the critical point of the phase transition which can distinguish the periodic lump chain and transformed wave. Therefore, we can conclude that the PINN method with a single phase transition parameter has a good prediction and ability for studying the state transition of waves. It is obvious in Fig. 4 that the absolute error of the PINN method is smaller than that of the DNN method.

Moreover, Table I shows the comparison between both methods more intuitively in terms of the relative L_2 error. When the value of the parameter q is equal to 0.8 or -0.5 , the prediction accuracy of the DNN method is slightly better than that of the PINN algorithm. However, with the parameter $q = 0.1$ or 0, the PINN method displays its superiority. By considering the overall factors (the cost of acquiring data, the relative L_2 error, and extrapolation performance), we believe that the PINN is a better choice for prediction of the phase transition for nonlinear waves.

Based on the above results, we conclude that the PINN method with a physical parameter can even replace analytical techniques for the investigation of the phase transition of waves, such as the Hirota method [72] and Darboux transformation [73]. We here discuss the difference and relation between both methods. For the analytical technique, the N -soliton solution can be converted into the periodic lump chain via the complexification technique. Such solution consists of the hyperbolic and trigonometric functions, which describe the locality and periodicity, respectively. Further,

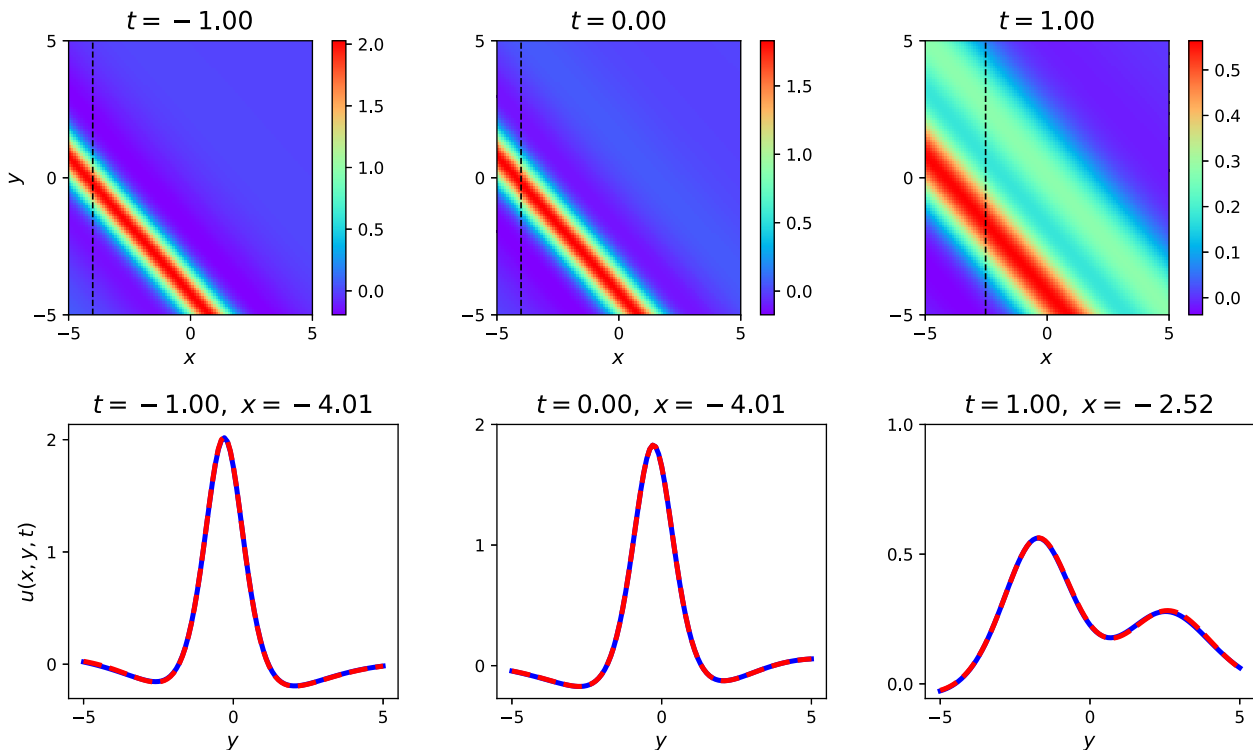


FIG. 10. Stability based on the W-shaped soliton. Top: The density plots of the predicted solution at different times. Bottom: The comparison between the predicted and exact solutions denoted by the dashed black lines. The solid blue line is the predicted solution, and the dashed red line is the exact one. Even if the initial data are doped with noise, the PINN method works well. The parameters are $\alpha = -1, \beta = -1, \gamma = 3$, and $\delta = 1$.

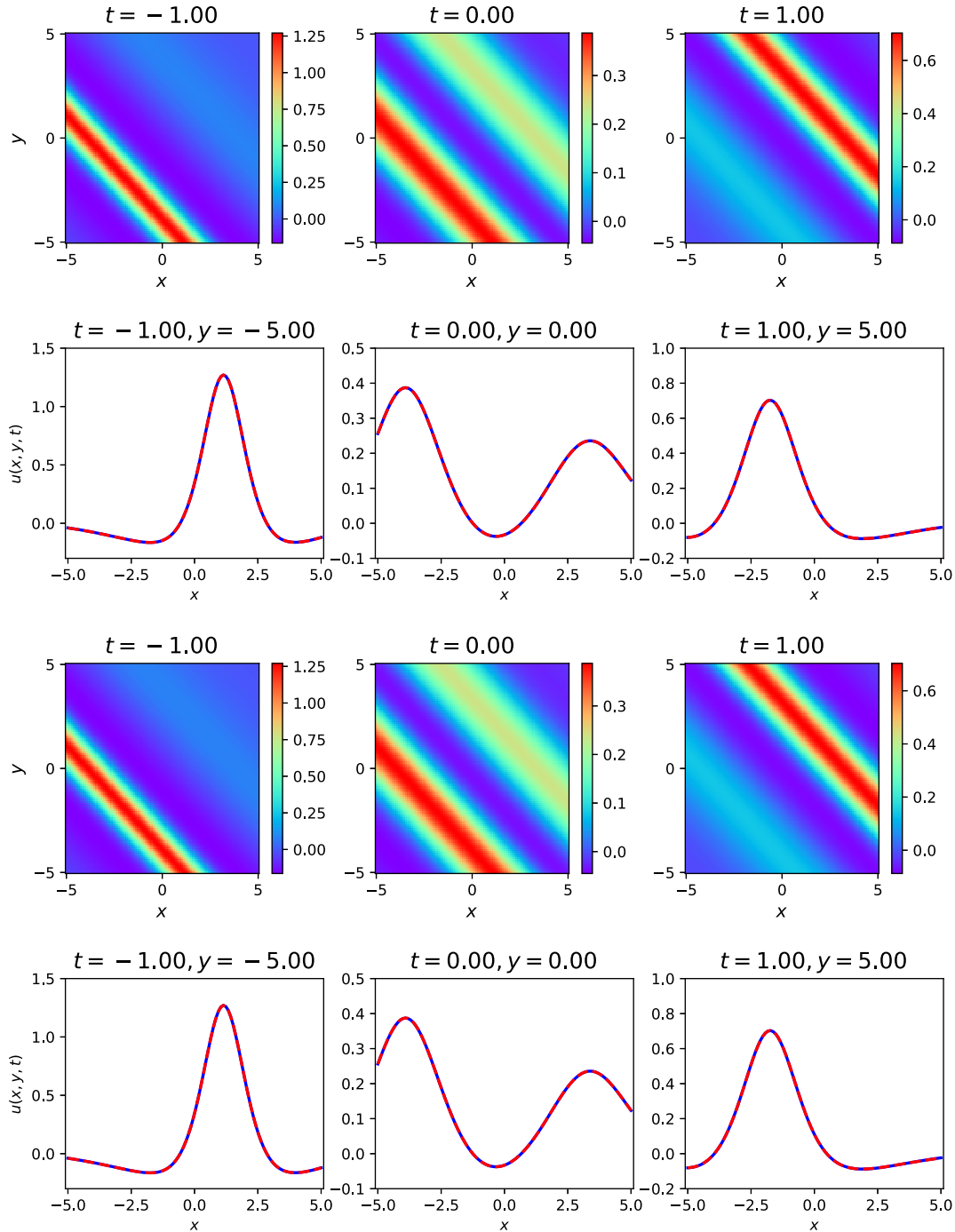


FIG. 11. Prediction of the M-shaped soliton. The plots in the first and second rows represent the density plots and comparison of the predicted result by training with noisy data based on the learned parameters α , β , and δ . Similarly, the third and fourth rows describe the density plots of the predicted result and comparison based on the learned parameter γ . The solid blue line is the exact solution, and the dashed red line is the predicted one. Obviously, the predicted results with noisy data are accurate based on the PINN method.

based on the analysis of characteristic lines, the mechanism of the phase transition can be revealed. If the characteristic lines for both wave components are parallel, the periodic lump chain can be transformed into various transformed waves, such as the solitary wave, multipeak soliton, and periodic wave. For the PINN algorithm, we only embed the physical parameter in the neural network as a substitute solution for the former. Based on highly accurate data (e.g., the exact solution

or numerical data), the trained neural network serves as a study of the mechanism of phase transition.

The analytical method mainly depends on the integrability of the model and the corresponding analytical tools. The crucial issue is to derive the solution as well as its mathematical analysis (as described above, the wave components, characteristic line, and phase shift analysis). For the PINN approach, we simply train a neural network with a phase transition

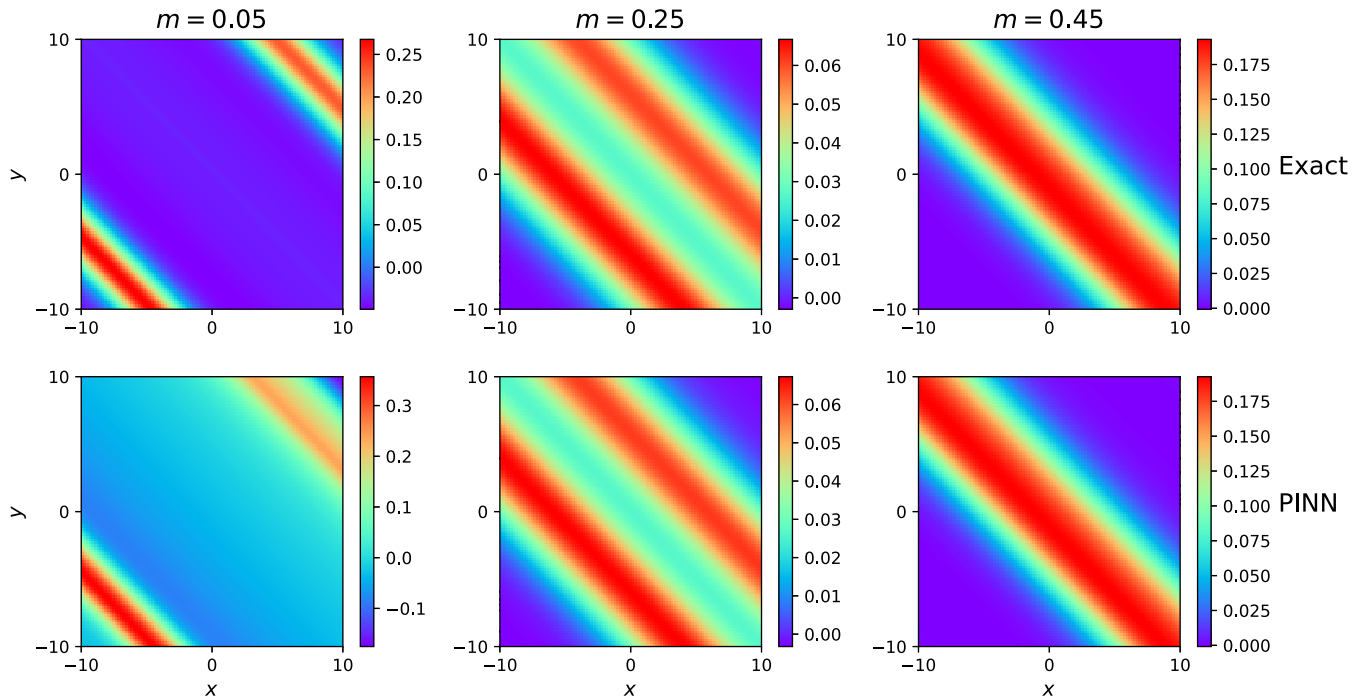


FIG. 12. Prediction of transformed waves on the dashed green line. The value of the parameter m in each column corresponds to the green star in Fig. 6. Each row of the plots is responsible for the exact and predicted results, respectively. The parameters are $\alpha = -1$, $\beta = -1$, $\gamma = 3$, and $\delta = 1$.

parameter to replace the complex mathematical analysis (the exact solution can be approximated by the neural network). Both can reveal the mechanism of the phase transition. However, in practical fields such as fluids, plasma, and nonlinear optics, numerous models are not integrable, in which case the analytical method fails. In contrast, the PINN technique shows its superiority. Notably, in the case where the training data are doped with noise or inaccurate (that is, without the exact solution), the PINN algorithm can still work well, which is impossible for the analytical methods relying heavily on integrability. Here, we verify the performance of the PINN technique by adding 10% noise to the initial data. From the experimental results in Fig. 5, even if the initial data are inaccurate, the PINN with a physical parameter still performs well in the prediction of the phase transition mechanism. Table II shows the relative L_2 errors for the above case, all of which are within the acceptable range.

IV. PREDICTION OF THE PHASE TRANSITION FOR TRANSFORMED WAVES

In the above section, we presented the exact boundary of the phase transition ($q = 0$). However, such network with a single parameter cannot distinguish the types of transformed waves. Thus, more physical parameters should be considered to address this issue, including the wave numbers of the solitary wave and periodic wave components (m and n). By adding these two parameters, the neural network has the intelligence to distinguish the localization and oscillation of the transformed waves, as we will see later.

To begin with, we train the PINN method with a single parameter (m or n) on the five different colors and styles

of lines. In Fig. 6, the dots and stars are the training and prediction points in five experiments, respectively. The predicted results and accuracy of these experiments are shown in Figs. 12–16 and Table VIII in Appendix B. When the value of the parameter n is set to 0.2 (the dashed green line), Fig. 12 exhibits the state that changes with the increase of the value of m , from a periodic wave to a W- or M-shaped soliton and then to a solitary wave. When the wave number of the periodic wave component is selected as $n = 0.7$ (the

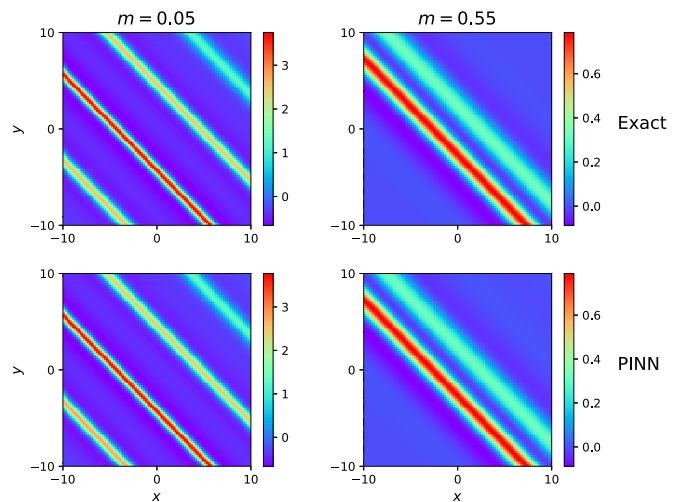


FIG. 13. Prediction of transformed waves on the densely dashed purple line. The value of the parameter m in each column corresponds to the purple star in Fig. 6. Each row of the plots is responsible for the exact and predicted results, respectively.

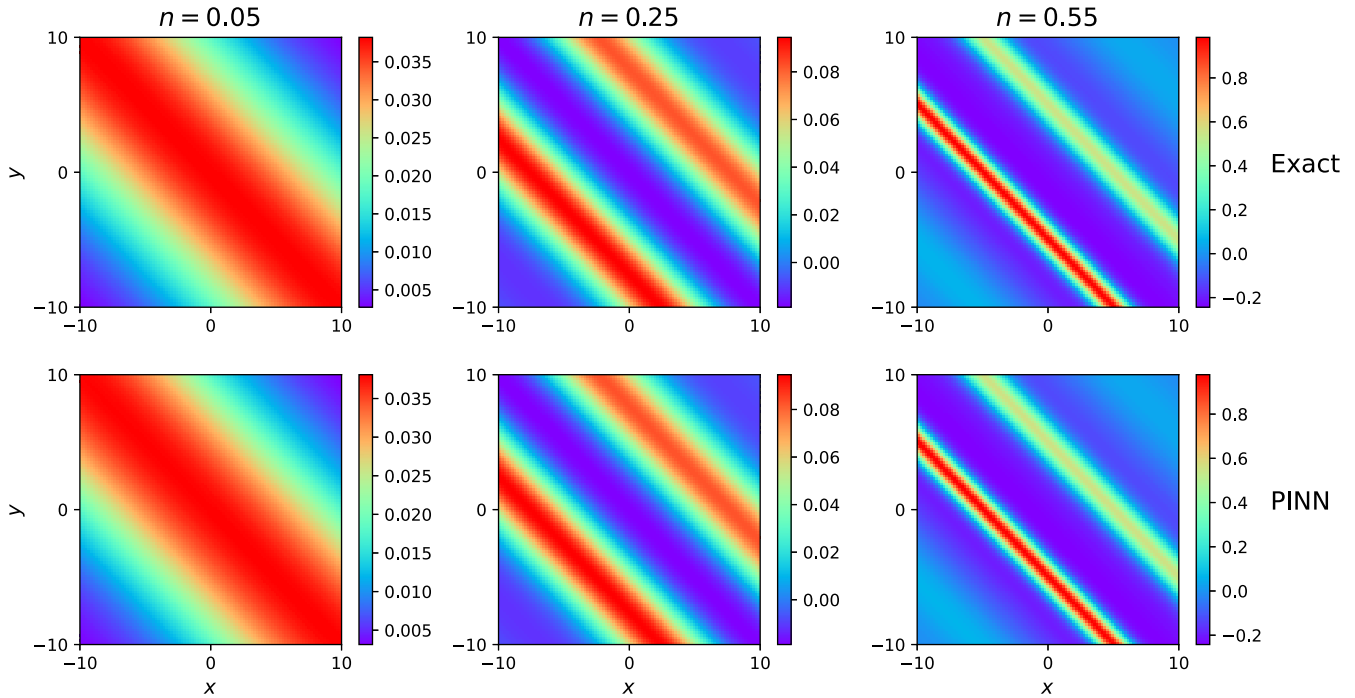


FIG. 14. Prediction of transformed waves on the solid red line. The value of the parameter n in each column corresponds to the red star in Fig. 6. Each row of the plots is responsible for the exact and predicted results, respectively.

densely dashed purple line), the transformed waves undergo a phase transition with the change of the parameter m , from a periodic wave to a W- or M-shaped soliton in Fig. 13. In addition, in the case where the wave number of the solitary wave component is fixed at $m = 0.2$ (the solid red line), it can be seen from the results in Fig. 14 that, when the value of parameter n varies, the transformed waves change accordingly, from a solitary wave to a W- or M-shaped soliton and then to a periodic wave. Similarly, if the value of m is equal to 0.6 (the dash-dotted blue line), we observe from Fig. 15 that, as

the wave number n increases, nonlinear waves are converted from a solitary wave to a W- or M-shaped soliton. Finally, we consider the dotted orange line in Fig. 6 that satisfies the condition $m^2 + n^2 = 0.36$. According to the experimental result in Fig. 16, when the ratio of the parameters m and n gradually decreases, that is, the value of the parameter m decreases, the transformed waves produce several states from a solitary wave to a W- or M-shaped soliton and then to a periodic wave.

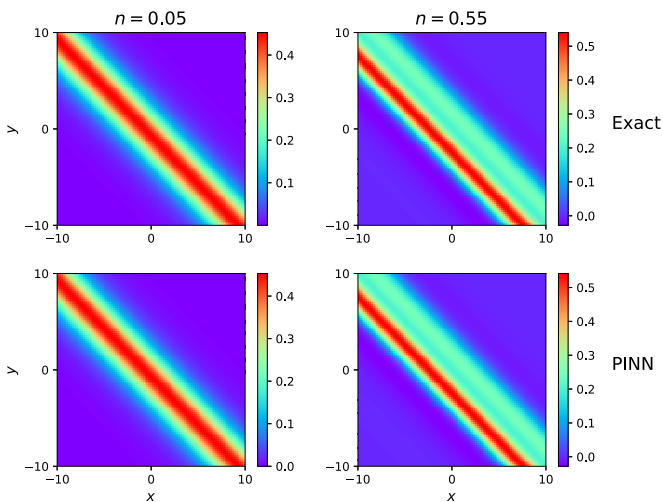


FIG. 15. Prediction of transformed waves on the dash-dotted blue line. The value of the parameter n in each column corresponds to the blue star in Fig. 6. Each row of the plots is responsible for the exact and predicted results, respectively.

From the results with a single parameter above, we note that the parameters m and n are responsible for the state of transformed waves. When the value of parameter n changes from 0.2 to 0.7, as shown in Figs. 12 and 13, the solitary waves disappear. As the value of the parameter m increases from 0.2 to 0.6, taking into account Figs. 14 and 15, the periodic waves are hard to observe. Based on these five experimental results, we speculate that when the ratio of the parameters m and n is large ($m \gg n$), the solitary waves exist in the corresponding region. If the ratio is close to 1 ($m \approx n$), the transformed waves appear in the W- and M-shaped states, and there exist periodic waves in the region where the ratio is small ($m \ll n$). Naturally, it is necessary to use the PINN method with two phase transition parameters to study such mechanism on the whole plane. However, the result obtained by the neural network learning data for a small number of locations (16 points) on the parameter plane is disappointing. We also tried to train the neural network with more location information, and finally found that the results are relatively satisfactory with the initial and boundary information of 49 points on the parameter plane (Fig. 7), but the cost of data from such a large amount of locations is too high. The previous experimental results on the lines suggest to us to consider the domain decomposition to tackle this issue.

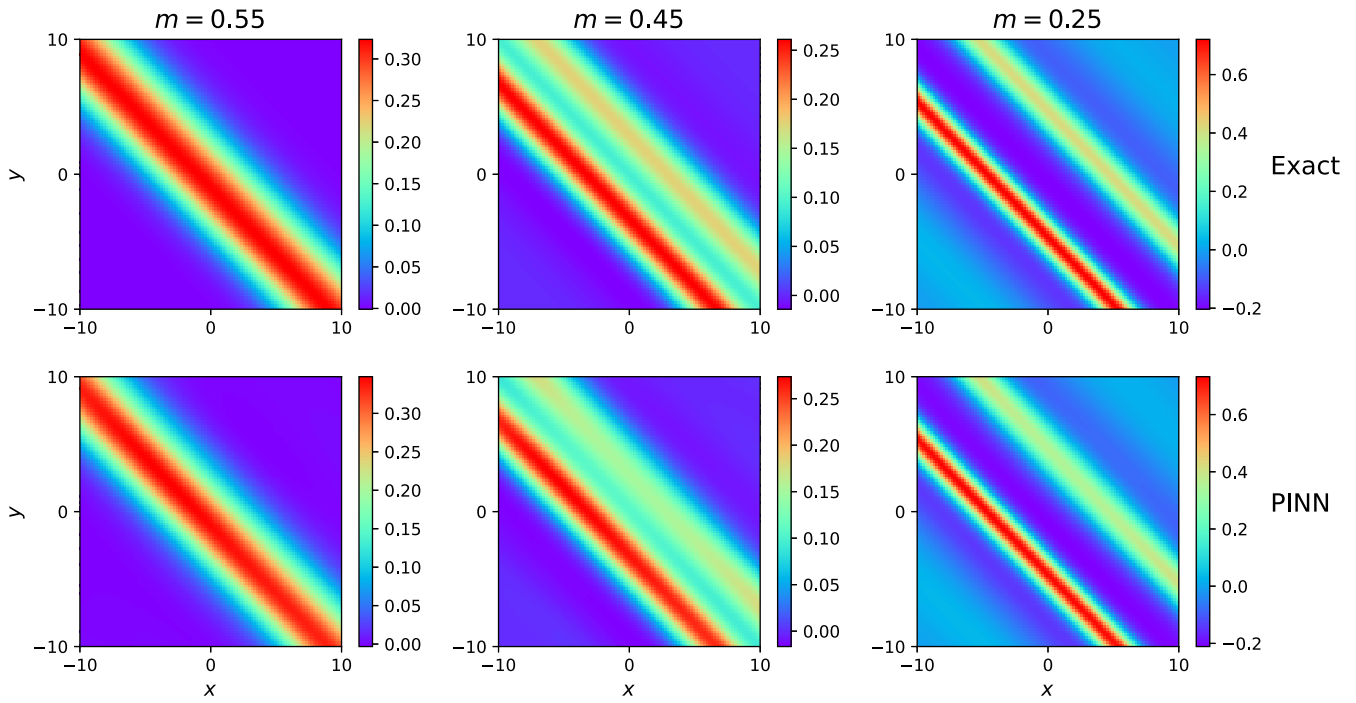


FIG. 16. Prediction of transformed waves on the dotted orange line. The value of the parameter m in each column corresponds to the orange star in Fig. 6. Each row of the plots is responsible for the exact and predicted results, respectively.

Fortunately, a previous study has addressed a similar issue. The extended PINN (decomposition of the space-time

domain to reduce the training cost [56]). It enables

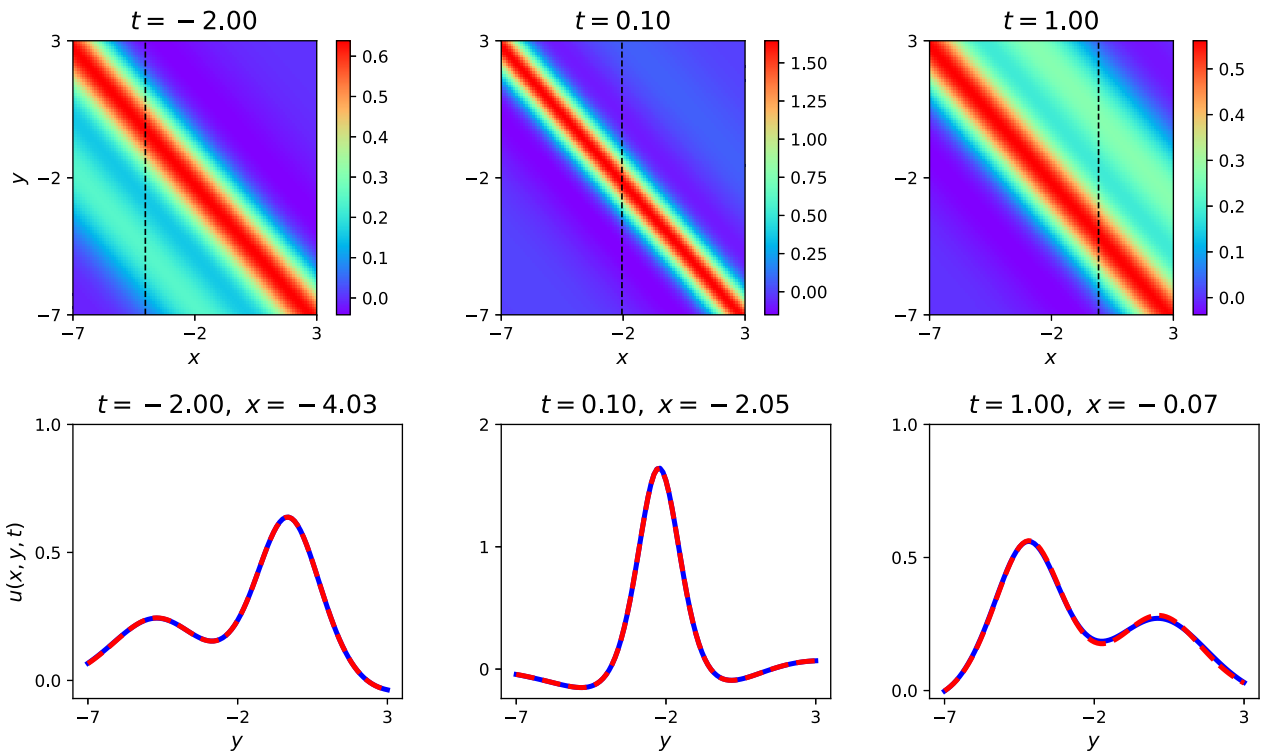


FIG. 17. Prediction of time-varying dynamics of the W-shaped soliton. Top: The density plots of the predicted solution at different times. Bottom: The comparison between the predicted and exact solutions denoted by the dashed black lines. The solid blue line is the predicted solution, and the dashed red line is the exact one. The PINN method has the ability to detect a new dynamical property, which successfully discovers the time-varying dynamics of Eq. (1). The parameters are $\alpha = -1$, $\beta = -1$, $\gamma = 3$, and $\delta = 1$.

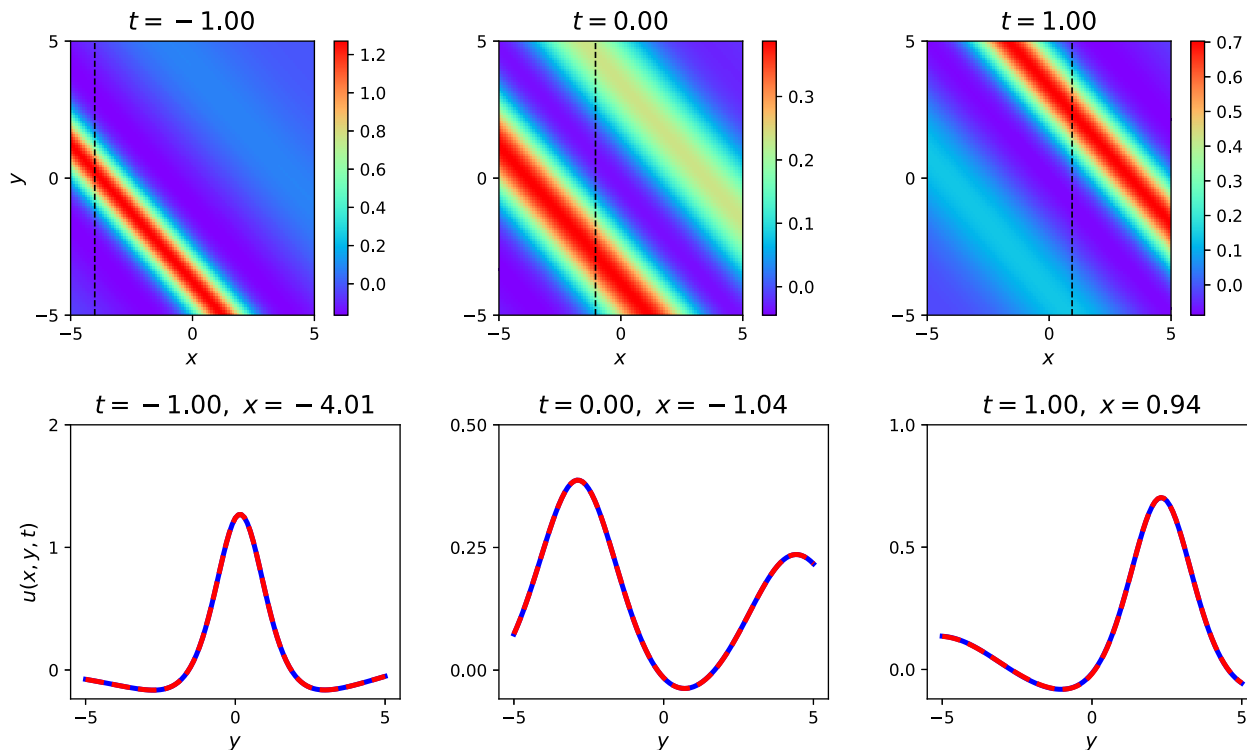


FIG. 18. Prediction of time-varying dynamics of the M-shaped soliton. Top: The density plots of the predicted solution at different times. Bottom: The comparison between the predicted and exact solutions denoted by the dashed black lines. The solid blue line is the predicted solution, and the dashed red line is the exact one. The parameters are $\alpha = -1$, $\beta = -1$, $\gamma = 3$, and $\delta = 1$.

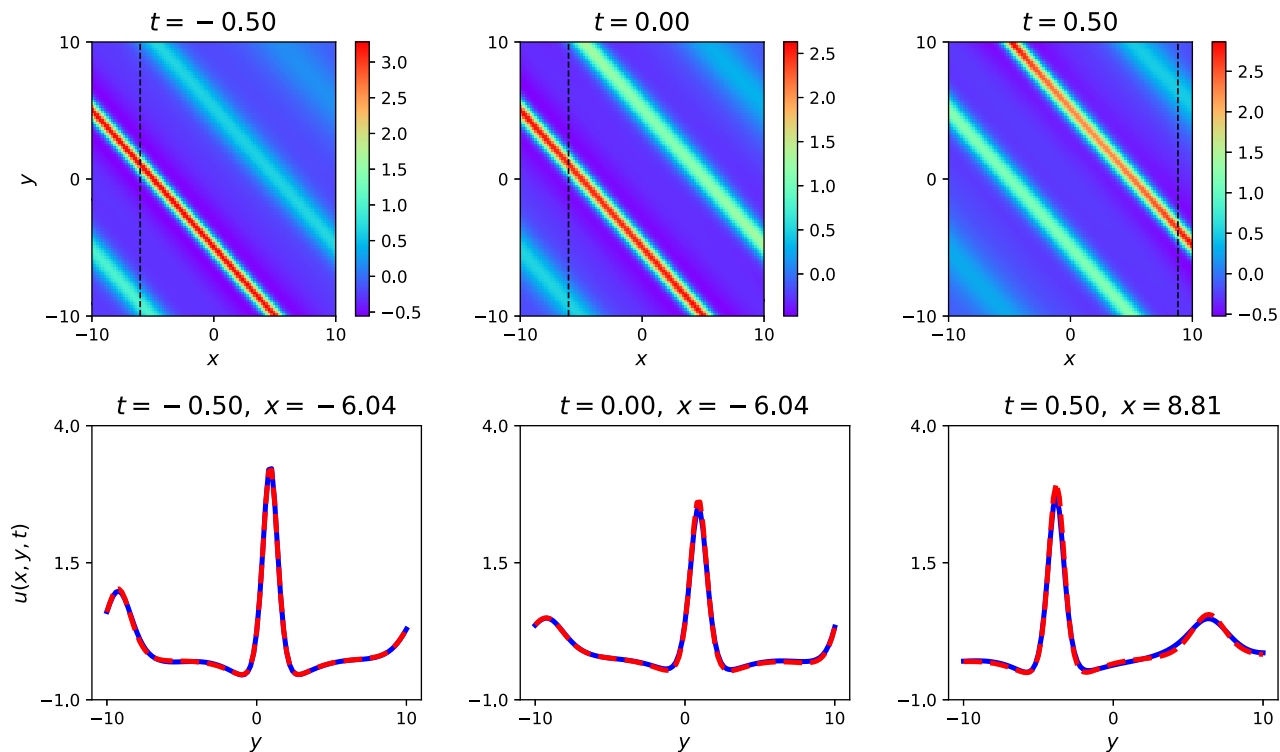


FIG. 19. Prediction of time-varying dynamics of the multipeak soliton. Top: The density plots of the predicted solution at different times. Bottom: The comparison between the predicted and exact solutions denoted by the dashed black lines. The solid blue line is the predicted solution, and the dashed red line is the exact one. The parameters are $\alpha = -1$, $\beta = -1$, $\gamma = 3$ and $\delta = 1$.

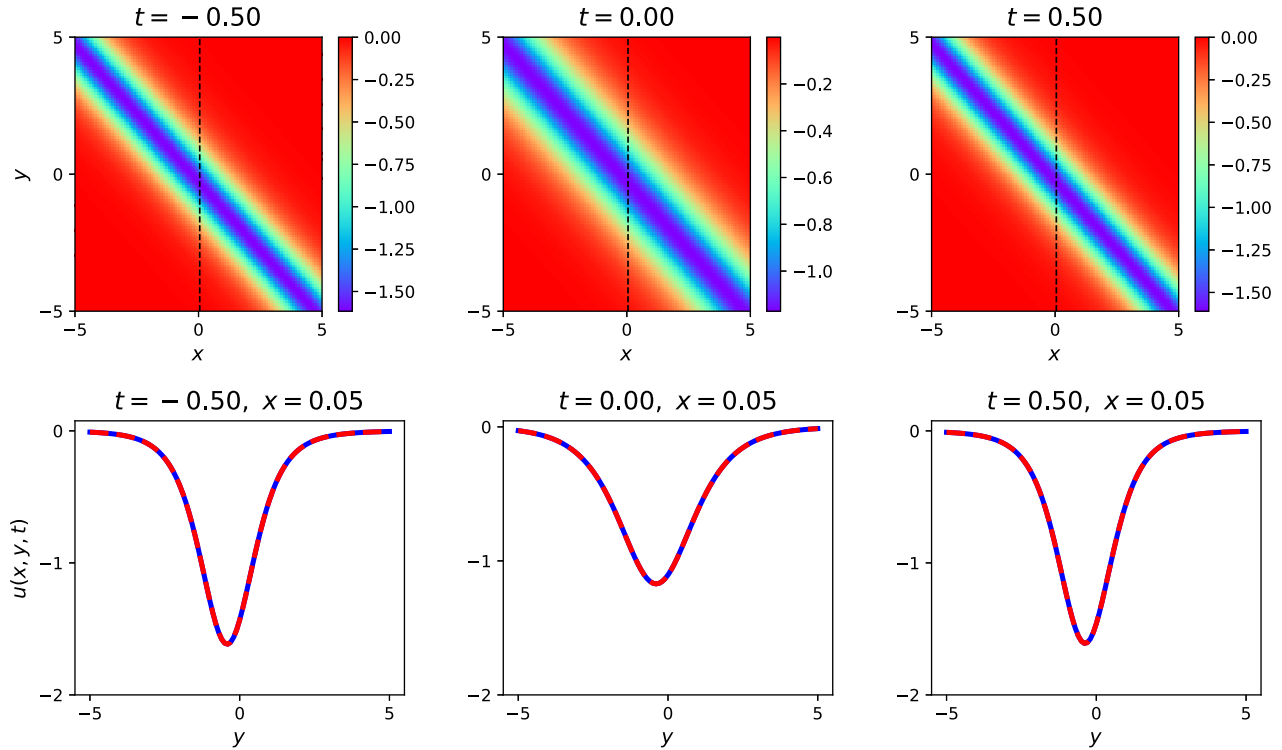


FIG. 20. Prediction of time-varying dynamics of the dark quasi-bell-shaped solitary wave. Top: The density plots of the predicted solution at different times. Bottom: The comparison between the predicted and exact solutions denoted by the dashed black lines. The solid blue line is the predicted solution, and the dashed red line is the exact one. The amplitude of the wave slightly changes, which indicates that the PINN method predicts the evolution of the dark solution well. The parameters are $\alpha = -8$, $\beta = 1$, $\gamma = -3$, and $\delta = 1$.

us to explore the boundaries of all kinds of transformed waves via the PINN method. Consequently, this problem may be solved effectively by designing the corresponding subdomains in different phase planes of the wave number. We hereby decompose the (m, n) plane into three subdomains in Fig. 8, namely, the blue domain (subdomain 1, $m \gg n$), green domain (subdomain 2, $m \approx n$), and pink domain (subdomain 3, $m \ll n$). Each one has a respective PINN with two phase transition parameters. We should point out that these boundaries are not strictly defined. In fact, it is a continuous state of the evolution for the transformed waves. Thus, whether it is based on the analytical methods or deep learning, we can only give the approximate boundaries of the phase transition.

As depicted in Fig. 8, we decompose the phase space into three subdomains. The data described by the dots are used to train the neural networks. The predicted solutions are generated from the data marked by the stars. At the location of the blue star in subdomain 1, the values of the parameters m and n are equal to 0.8 and 0.01 ($m \gg n$), respectively. The position where the values of the parameters both equal 0.6 ($m \approx n$) is marked by the green star in subdomain 2. The red star in subdomain 3 stands for the case that the values of the parameters m and n are equal to 0.1 and 0.6 ($m \ll n$), respectively. Based on the neural networks, the dynamical process of the point in the (m, n) plane can be predicted. We build a separate PINN framework with two phase transition parameters in different regions. Specifically, $\mathbf{x}^0 = \{x, y, t, m, n\}$ is the input of the neural networks. The values of the parameters m and n are

responsible for the wave numbers of the solitary wave and periodic wave components, respectively.

In order to confirm the practicability of the pPINN method, we display the states of transformed waves with different values of the parameters m and n at a fixed time, shown in Fig. 9. The coordinates of the blue star, green star, and red star in Fig. 8 correspond to the values of the parameters m and n in each column, respectively. In particular, the dynamical solutions with these groups of parameters are not used to train the networks in the corresponding regions. As shown in the first row, the patterns of exact solutions with different groups of parameters m and n are described. We find that the state of transformed waves appears to change from a quasisolitary wave to a M-shaped soliton and then to a multipeak soliton. The plots in the second and third rows depict the predicted results of the PINN and DNN algorithms, respectively. Further, we give the absolute errors between the exact and predicted solutions from both algorithms in the last two lines. In addition, the plots in the first column in Fig. 9 show the pattern of the quasisolitary wave when the value of the parameter m is much larger than that of the parameter n . In the second column, it can be found that the M-shaped soliton state appears if the value of the parameter m approximates that of the parameter n . Furthermore, when the value of the parameter m is much smaller than that of the parameter n , the multipeak soliton is depicted in the third column. In addition, from the absolute error analysis, the PINN method is better than the DNN for predicting the quasisolitary wave and M-shaped soliton. In order to more clearly compare the

TABLE IV. The relative L_2 errors of the predicted result under initial data with noise.

Types	$t = -1$	$t = 0$	$t = 1$
The relative L_2 error	4.37477×10^{-3}	1.504691×10^{-3}	1.122544×10^{-2}

predicted results of both methods, Table III is presented. We find that the relative L_2 errors of the PINN method are smaller than those of the DNN method for the predicted results of dynamical solutions marked by star points. Hence, for the phase transition of transformed waves, the predicted results of the PINN are superior to the DNN.

Finally, we discuss the boundaries of the phase transition based on the pPINN algorithm. In fact, we can predict similar patterns of nonlinear waves in the neighborhood of each star point in the (m, n) plane, such as the quasisolitary wave, W- or M-shaped soliton, and multipeak soliton. According to the above results, we find that the PINN method can provide a reasonable explanation for analysis of the wave components behind the transformed wave. Under the condition that the value of the parameter m is larger than that of n , the pattern of the wave exhibits a stronger solitary state and a weaker periodic state. If the condition becomes the opposite of the above, the wave with a weaker solitary state and a stronger periodic state is characterized. In addition, when the value of the parameter m is not equal to zero and that of n is equal to zero, the solitary wave will appear. When the above case is reversed, we can observe the periodic wave, and in the neighborhood of the origin in the (m, n) plane a line rogue wave will be gradually generated. Here, we can divide the approximate boundaries of the phase transition of different types of transformed waves in the (m, n) plane by the pPINN method with two parameters.

Moreover, based on the experiments on the lines, we simulate and analyze the locality and oscillation of transformed waves. Further, we can observe two transformed waves (the positions of the triangles in Fig. 8) with approximately the same such physical characteristics (locality and oscillation). According to the coordinates of two triangles, the boundary between the W- or M-shaped soliton and periodic wave can be divided approximately. If characteristics (locality and oscillation) at two positions are distinctively different, we will continue to explore other transformed waves on the

line, until we find a suitable one. In fact, the boundary between the solitary wave and W- or M-shaped soliton can be also defined in the same way as above (the positions of the squares in Fig. 8). In particular, we need to point out that because the transformed wave is a continuous state of the evolution, whether using the PINN or analytical methods, the results obtained are the inexact boundaries. Thus, the PINN method can serve as an effective technique for studying the phase transition of different types of transformed waves.

V. PREDICTION OF THE TIME-VARYING PROPERTY

In this section, according to the predicted results of the phase transition above and the data derived from the soliton solution [66], we explore a dynamics characteristic of the $(2 + 1)$ -dimensional Boussinesq equation. Here, we are mainly interested to understand the predictive ability of the PINN in the evolutionary dynamics of phase transition solutions. In particular, for several experiments in this part, we select the internal collocation points using the latin hypercube sampling (LHS) strategy [74]. The experimental results are exhibited in Figs. 17–20 and Table IX in Appendix C.

In Figs. 17 and 18, we demonstrate the evolution of the W- and M-shaped solitons with time. Obviously, based on the predicted condition of the phase transition above (namely, $q = 0$), we can clearly observe a solitary wave state instead of a periodic lump chain. Further, according to the results of Sec. IV, by considering the ratio of the parameters m and n , we see that the W-shaped soliton appears alternately with the M-shaped one. The W-shaped soliton has a high main peak and two valleys. Over time, it becomes the M-shaped soliton with two peaks. Specifically, the deformation always occurs during the propagation of the wave. Further, in Fig. 19, the prediction of propagation of the multipeak soliton is described in detail. The shape-changed propagation of such wave is also observed (the peaks as well as their amplitudes of the

TABLE V. The predicted values and the error rates of the parameters α , β , and δ , and the relative L_2 errors of the predicted results.

Types	Data	Exact	0% noise	1% noise
α		1	1.0902245	1.089022
Error rate for α		0	9.02245%	8.9022045%
β		1	0.9146659	0.9246567
Error rate for β		0	8.533412%	7.5343313%
δ		1	0.9977599	0.98968667
Error rate for δ		0	0.22401214%	1.03133327%
The relative L_2 error	$t = -1$	0	4.431319×10^{-4}	1.080991×10^{-3}
	$t = 0$	0	6.389340×10^{-4}	8.097205×10^{-4}
	$t = 1$	0	1.215457×10^{-3}	1.939527×10^{-3}

TABLE VI. The predicted value and the error rate of the parameter γ , and the relative L_2 errors of the predicted results.

Types \ Data		Exact	0% noise	1% noise
γ		3	3.009863	3.000359
Error rate for γ		0	0.3287633%	0.01196861%
The relative L_2 error	$t = -1$	0	5.152031×10^{-4}	8.157609×10^{-4}
	$t = 0$	0	6.9918606×10^{-4}	9.019213×10^{-4}
	$t = 1$	0	1.8393467×10^{-3}	3.2545326×10^{-3}

multipeak soliton change dramatically). However, the locality and oscillation of the wave remain unchanged with time. This suggests that the PINN algorithm accurately predicts a more complicated evolution behavior of the wave (the wave with strong oscillation and multiple peaks). Figure 20 describes the predicted result of the dark quasi-bell-shaped solitary wave. We note that the amplitude of the wave changes slightly with time. Apparently, it resembles the evolution of a soliton, but its analytical expression consists of both hyperbolic and trigonometric functions, so it deforms slightly as it propagates. It can be confirmed that the PINN method still has a good learning ability for studying the state of the quasisolution (also a dark soliton).

Notably, by using the data derived from the soliton solution and the phase transition condition, we successfully use the PINN to explore the dynamical mechanism for Eq. (1), that is, the time-varying property. It is indicated that the PINN method is not only useful in the prediction of phase transition, but also effective in detecting the mechanism of the dynamical solution. Thus, we recognize that the PINN method can predict accurately the dynamical evolution of such waves. It is worth noting that previous studies have used the PINN method to predict the evolution of stable soliton states with unchanged profiles [59,60]. Here, our results show that this

technique can work well for the dynamics of the waves with the shape-changed propagation.

VI. STABILITY

In the above sections, we studied the phase transition mechanism of transformed waves as well as their time-varying dynamics by using the PINN method. Importantly, the stability of the technique is also a question that has received much concern. Next, we will focus on its stability based on the initial data with noise.

We use the PINN technique to discuss the W-shaped soliton of Eq. (1) numerically. The internal collocation points are selected through the LHS strategy [74]. In addition, we add 10% noise to the initial data extracted to observe the influence of noise.

We depict Fig. 10, which represents the density plots of the predicted result and the comparison between the exact and predicted solutions, where the blue solid line is the predicted solution and the red dotted line is the exact solution. In addition, in terms of accuracy of the predicted results, we give the relative L_2 errors at different times in Table IV. By adding noise to the initial data, the PINN method not only still predicts the soliton state, but also shows the time-varying

TABLE VII. Network structure, training data set, and spatiotemporal domain.

Types		Hidden layers	Neurons	Initial data	Boundary data	Collocation points	Spatiotemporal domain
Section 3	Section 3	6	40	4000	8000	10000	$[-5, 5] \times [-5, 5] \times [-0.5, 0.5]$
	Dashed green line	5	50	4000	8000	10000	$[-10, 10] \times [-10, 10] \times [-0.5, 0.5]$
	Densely dashed purple line	5	50	4000	8000	10000	$[-10, 10] \times [-10, 10] \times [-0.5, 0.5]$
Section 4	Solid red line	5	50	4000	8000	10000	$[-10, 10] \times [-10, 10] \times [-0.5, 0.5]$
	Dash-dotted blue line	5	50	4000	8000	10000	$[-10, 10] \times [-10, 10] \times [-0.5, 0.5]$
	Dotted orange line	5	50	4000	8000	10000	$[-10, 10] \times [-10, 10] \times [-0.5, 0.5]$
	Subdomain 1	5	50	4000	8000	20000	$[-5, 5] \times [-5, 5] \times [-0.5, 0.5]$
	Subdomain 2	5	50	4000	8000	40000	$[-5, 5] \times [-5, 5] \times [-0.5, 0.5]$
	Subdomain 3	5	50	4000	8000	40000	$[-10, 10] \times [-10, 10] \times [-0.5, 0.5]$
	W-shaped soliton	5	30	1000	4000	2000	$[-7, 3] \times [-7, 3] \times [-2, 1]$
M-shaped soliton	5	30	1000	4000	2000	$[-5, 5] \times [-5, 5] \times [-1, 1]$	
Section 5	Multipeak soliton	5	30	3000	4000	5000	$[-10, 10] \times [-10, 10] \times [-0.5, 0.5]$
	Dark quasi-bell-shaped solitary wave	5	30	1000	4000	2000	$[-5, 5] \times [-5, 5] \times [-0.5, 0.5]$
	Section 6	5	30	1000	4000	2000	$[-5, 5] \times [-5, 5] \times [-1, 1]$
	Section 7	5	40	2000	4000	5000	$[-5, 5] \times [-5, 5] \times [-1, 1]$

TABLE VIII. The relative L_2 errors of the predicted results at $t = 0$.

Types		The relative L_2 error
Dashed green line ($n = 0.2$)	$m = 0.05$	6.079395×10^{-1}
	$m = 0.25$	1.816038×10^{-2}
	$m = 0.45$	7.945124×10^{-3}
Densely dashed purple line ($n = 0.7$)	$m = 0.05$	3.634826×10^{-2}
	$m = 0.55$	7.570973×10^{-3}
	$n = 0.05$	8.854506×10^{-3}
Solid red line ($m = 0.2$)	$n = 0.25$	6.270758×10^{-3}
	$n = 0.55$	8.264634×10^{-3}
	$n = 0.05$	1.418518×10^{-3}
Dash-dotted blue line ($m = 0.6$)	$n = 0.55$	3.566368×10^{-3}
	$n = 0.05$	4.919089×10^{-2}
Dotted orange line ($m^2 + n^2 = 0.36$)	$m = 0.55$	6.382458×10^{-2}
	$m = 0.45$	6.312821×10^{-2}
	$m = 0.25$	

dynamics quite well. It is further observed that the algorithm has robustness for noise.

VII. DATA-DRIVEN PARAMETERS DISCOVERY

Finally, by utilizing the PINN technique, we focus on the inverse problem of the $(2 + 1)$ -dimensional Boussinesq equation with the M-shaped soliton, namely, the data-driven parameters discovery:

$$u_{tt} + \alpha u_{xx} + \beta u_{yy} - \gamma (u^2)_{xx} - \delta u_{xxxx} = 0. \quad (11)$$

Specifically, we mainly study the parameters of the dispersion and nonlinear terms of Eq. (11), i.e., α , β , γ , and δ . Based on the PINN algorithm [51], these parameters can be learned by minimizing the loss function. This loss function is composed of three components, namely, the initial condition, boundary condition, and penalty at internal collocation points, which are the same as in Sec. II.

In order to show the feasibility of this algorithm for studying the inverse problem of the shallow water wave equation in the high-dimensional case [i.e., Eq. (11)], we construct the sample as well as the exact solution corresponding to the parameters $\alpha = 1$, $\beta = 1$, $\gamma = 3$, and $\delta = 1$. Zero initialization is adopted for the unknown parameters to be learned before training. In addition, the key is optimizing the weights and biases of the neural network, which is based on constructing the data set to minimize the loss function by employing the Adam [70] and L-BFGS [71] optimization algorithms.

The predicted results of the unknown parameters are displayed in Tables V and VI. When the value of the parameter γ is fixed to 3, the results are shown in Table V. Table VI displays results for the case in which the values of the parameters α , β , and δ are equal to 1, 1, and 1, respectively. Regardless of whether the training data include noise, the accuracy of the predicted results is within an acceptable range. In particular, for the data-driven parameters discovery, the predicted values are as close as possible to the target values and the error rates are all below 10% (the error rate is defined as $\frac{|\alpha_{\text{pred}} - \alpha_{\text{exact}}|}{\alpha_{\text{exact}}} \times 100\%$). The relative L_2 errors of the predicted solution are on the order of 10^{-3} or 10^{-4} at differ-

ent times ($t = -1, 0$, and 1). Consequently, we can conclude that the PINN method can effectively identify the unknown parameters of Eq. (11) and accurately predict the dynamical evolution of the M-shaped soliton.

Figure 11 shows the predicted result of the M-shaped soliton solution for Eq. (11). The top part gives the evolution mechanism of the M-shaped soliton and the comparison between the predicted and exact solutions (in the case of fixed variables t and y), based on the learned parameters of the dispersion terms. The bottom part depicts the predicted solution and the comparison for the training data with noise based on the learned parameter γ . From the perspective of visualization, it is proved that the PINN method can effectively capture the time-varying evolution of the M-shaped soliton and learn unknown parameters well.

VIII. CONCLUSION

In this paper, we focused on the $(2 + 1)$ -dimensional Boussinesq equation describing the propagation of waves in opposite directions on the surface of water. First, based on the PINN method with a physical parameter, we found the exact boundary of the phase transition which distinguishes the periodic lump chain and transformed wave. More specifically, we suggested that transformed waves appear if and only if $q = 0$, while the other points cannot be responsible for such phenomenon. In addition, the phase transition of different types of transformed waves was studied on the parameter lines and (m, n) plane. We discovered that the bell-shaped solitary waves appear when the value of m is obviously greater than that of n . Instead, multipeak solitons are generated. Under the case in which both m and n are close in value, the M- and W-shaped profiles can be observed. By comparing the predicted results between the PINN and DNN methods, it can be seen that the former result with a physical constraint is better than the latter. Further, through the phase transition condition and the data obtained after assisted processing of the soliton solution in Ref. [66], we found types of solutions and a dynamical property of the $(2 + 1)$ -dimensional Boussinesq equation, namely, time-varying dynamics. We also discussed stability by adding some noise to the initial data based on the

TABLE IX. The relative L_2 errors of the predicted results at different times.

Types	The relative L_2 error		
W-shaped soliton	3.536170×10^{-3}	1.383507×10^{-3}	1.693224×10^{-2}
M-shaped soliton	6.375637×10^{-4}	8.127553×10^{-4}	3.428113×10^{-3}
Multipeak soliton	2.367967×10^{-2}	7.943103×10^{-2}	1.517877×10^{-1}
Dark quasi-bell-shaped solitary wave	2.588961×10^{-4}	1.021708×10^{-4}	3.463948×10^{-4}

PINN technique. We learn from the results that such method has a certain robustness for noise. Finally, we investigated the parameters discovery of the dispersion and nonlinear terms for Eq. (11) with and without noise, respectively. Our results showed that the PINN algorithm has a good prediction ability for studying the high-dimensional water wave equation in opposite directions, and the solutions and physical mechanisms can be predicted with only a small amount of simple data. It should be noted that an analytical scheme is also being studied for the state transition mechanism of Eq. (1) [75].

The data that support the findings of this paper are available from the corresponding author upon reasonable request. The codes in this paper are available in Ref. [76].

ACKNOWLEDGMENTS

We express our sincere thanks to the referees for their valuable comments. This work has been supported by the National Natural Science Foundation of China under Grants No. 12375002, No. 52076074, and No. 12205029.

H.L. cowrote the paper and code and performed simulations, calculations, and analysis. L.W. conceived the idea, cowrote the paper and algorithm, and performed the total design scheme and analysis. Y.Z. cowrote the code. G.L. cowrote the paper and performed the analysis. L.L. cowrote the paper and performed the analysis.

APPENDIX A: IMPLEMENTATION DETAILS

In this part, we show the details of all experiments in this paper. In order to deal with the nonlinearity and high-order dispersion terms of the equation, we adopt the number of hidden layers of the neural network and neurons in each layer appropriately. In addition, the configurations of the network structure and collocation points need to be adjusted, in response to the characteristics of the model, the complexity of nonlinear waves, and the range of the domain. In the following, based on certain experiments, we present the network structure and collocation points that are suitable for Eq. (1), as shown in Table VII.

APPENDIX B: EXPERIMENTS ON THE LINES

Here, we present the results predicted by the PINN method with a single parameter and prediction accuracy on five different lines in Fig. 6 (see Figs. 12–16 and Table VIII).

APPENDIX C: EXPERIMENTS ON THE TIME-VARYING WAVES

In this part, the predictions of the time-varying dynamics of the transformed waves are shown, in Figs. 17–20 and Table IX.

-
- [1] M. J. Ablowitz and P. A. Clarkson, *Solitons, Nonlinear Evolution Equations and Inverse Scattering* Vol. 149 (Cambridge University, New York, 1991).
 - [2] A. Chabchoub, N. P. Hoffmann, and N. Akhmediev, Rogue wave observation in a water wave tank, *Phys. Rev. Lett.* **106**, 204502 (2011).
 - [3] Y. V. Bludov, V. V. Konotop, and N. Akhmediev, Matter rogue waves, *Phys. Rev. A* **80**, 033610 (2009).
 - [4] L. Wen, L. Li, Z. D. Li, S. W. Song, X. F. Zhang, and W. M. Liu, Matter rogue wave in Bose-Einstein condensates with attractive atomic interaction, *Eur. Phys. J. D* **64**, 473 (2011).
 - [5] P. S. Vinayagam, R. Radha, and K. Porsezian, Taming rogue waves in vector Bose-Einstein condensates, *Phys. Rev. E* **88**, 042906 (2013).
 - [6] N. J. Zabusky and M. D. Kruskal, Interaction of “solitons” in a collisionless plasma and the recurrence of initial states, *Phys. Rev. Lett.* **15**, 240 (1965).
 - [7] H. Bailung, S. K. Sharma, and Y. Nakamura, Observation of peregrine solitons in a multicomponent plasma with negative ions, *Phys. Rev. Lett.* **107**, 255005 (2011).
 - [8] B. Kibler, J. Fatome, C. Finot, G. Millot, F. Dias, G. Genty, N. Akhmediev, and J. M. Dudley, The Peregrine soliton in nonlinear fibre optics, *Nat. Phys.* **6**, 790 (2010).
 - [9] D. R. Solli, C. Ropers, P. Koonath, and B. Jalali, Optical rogue waves, *Nature (London)* **450**, 1054 (2007).
 - [10] H. Li, C. Liu, Z. Y. Yang, and W. L. Yang, Quantized Superfluid Vortex Filaments Induced by the Axial Flow Effect, *Chin. Phys. Lett.* **37**, 030302 (2020).
 - [11] H. Li, C. Liu, W. Zhao, Z. Y. Yang, and W. L. Yang, Breather-induced quantised superfluid vortex filaments and their characterisation, *Commun. Theor. Phys.* **72**, 075802 (2020).
 - [12] M. G. Copus and R. E. Camley, Creation of magnetic rogue waves, *Phys. Rev. B* **102**, 220410(R) (2020).
 - [13] G. P. Agrawal, Nonlinear fiber optics, in *Nonlinear Science at the Dawn of the 21st Century* (Springer, New York, 2000), p. 195.
 - [14] J. M. Dudley, F. Dias, M. Erkintalo, and G. Genty, Instabilities, breathers and rogue waves in optics, *Nat. Photonics* **8**, 755 (2014).

- [15] A. Chabchoub, B. Kibler, J. M. Dudley, and N. Akhmediev, Hydrodynamics of periodic breathers, *Phil. Trans. R. Soc. A* **372**, 20140005 (2014).
- [16] B. Kibler, J. Fatome, C. Finot, G. Millot, G. Genty, B. Wetzell, N. Akhmediev, F. Dias, and J. M. Dudley, Observation of Kuznetsov-Ma soliton dynamics in optical fibre, *Sci. Rep.* **2**, 463 (2012).
- [17] D. H. Peregrine, Water waves, nonlinear Schrödinger equations and their solutions, *J. Aust. Math. Soc. Series B, Appl. Math.* **25**, 16 (1983).
- [18] K. L. Henderson, D. H. Peregrine, and J. W. Dold, Unsteady water wave modulations: Fully nonlinear solutions and comparison with the nonlinear Schrödinger equation, *Wave Motion* **29**, 341 (1999).
- [19] C. Kharif, E. Pelinovsky, and A. Slunyaev, *Rogue Waves in the Ocean* (Springer, New York, 2008).
- [20] V. I. Shrira and V. V. Geogjaev, What makes the Peregrine soliton so special as a prototype of freak waves? *J. Eng. Math.* **67**, 11 (2010).
- [21] N. Akhmediev, A. Ankiewicz, and M. Taki, Waves that appear from nowhere and disappear without a trace, *Phys. Lett. A* **373**, 675 (2009).
- [22] D. J. Korteweg and G. De Vries, On the change of form of long waves advancing in a rectangular canal, and on a new type of long stationary waves, *Lond. Edinb. Dublin philos. mag. J. Sci.* **39**, 422 (1895).
- [23] V. E. Zakharov, Stability of periodic waves of finite amplitude on the surface of a deep fluid, *J. Appl. Mech. Tech. Phys.* **9**, 190 (1968).
- [24] R. Hirota, Exact N-soliton solutions of the wave equation of long waves in shallow-water and in nonlinear lattices, *J. Math. Phys.* **14**, 810 (1973).
- [25] Y. Ohta and J. K. Yang, Rogue waves in the Davey-Stewartson I equation, *Phys. Rev. E* **86**, 036604 (2012).
- [26] W. X. Ma, Lump solutions to the Kadomtsev-Petviashvili equation, *Phys. Lett. A* **379**, 1975 (2015).
- [27] Z. Wang, Modelling nonlinear electrohydrodynamic surface waves over three-dimensional conducting fluids, *Proc. R. Soc. A* **473**, 20160817 (2017).
- [28] E. Falcon, C. Laroche, and S. Fauve, Observation of depression solitary surface waves on a thin fluid layer, *Phys. Rev. Lett.* **89**, 204501 (2002).
- [29] J. Y. Dong, L. M. Ling, and X. E. Zhang, Kadomtsev-Petviashvili equation: One-constraint method and lump pattern, *Physica D* **432**, 133152 (2022).
- [30] F. Baronio, S. Wabnitz, and Y. Kodama, Optical kerr spatiotemporal dark-lump dynamics of hydrodynamic origin, *Phys. Rev. Lett.* **116**, 173901 (2016).
- [31] J. G. Rao, K. W. Chow, D. Mihalache, and J. S. He, Completely resonant collision of lumps and line solitons in the Kadomtsev-Petviashvili I equation, *Stud. Appl. Math.* **147**, 1007 (2021).
- [32] C. Lester, A. Gelash, D. Zakharov, and V. Zakharov, Lump chains in the KP-I equation, *Stud. Appl. Math.* **147**, 1425 (2021).
- [33] A. Chowdury, A. Ankiewicz, and N. Akhmediev, Moving breathers and breather-to-soliton conversions for the Hirota equation, *Proc. R. Soc. A* **471**, 20150130 (2015).
- [34] A. Chowdury, D. J. Kedziora, A. Ankiewicz, and N. Akhmediev, Breather-to-soliton conversions described by the quintic equation of the nonlinear Schrödinger hierarchy, *Phys. Rev. E* **91**, 032928 (2015).
- [35] C. Liu, Z. Y. Yang, L. C. Zhao, and W. L. Yang, State transition induced by higher-order effects and background frequency, *Phys. Rev. E* **91**, 022904 (2015).
- [36] C. Liu, Z. Y. Yang, L. C. Zhao, and W. L. Yang, Transition, coexistence, and interaction of vector localized waves arising from higher-order effects, *Ann. Phys. (NY)* **362**, 130 (2015).
- [37] L. Wang, J. H. Zhang, Z. Q. Wang, C. Liu, M. Li, F. H. Qi, and R. Guo, Breather-to-soliton transitions, nonlinear wave interactions, and modulational instability in a higher-order generalized nonlinear Schrödinger equation, *Phys. Rev. E* **93**, 012214 (2016).
- [38] L. Wang, J. H. Zhang, C. Liu, M. Li, and F. H. Qi, Breather transition dynamics, Peregrine combs and walls, and modulation instability in a variable-coefficient nonlinear Schrödinger equation with higher-order effects, *Phys. Rev. E* **93**, 062217 (2016).
- [39] J. H. Zhang, L. Wang, and C. Liu, Superregular breathers, characteristics of nonlinear stage of modulation instability induced by higher-order effects, *Proc. R. Soc. A* **473**, 20160681 (2017).
- [40] L. Wang, X. Wu, and H. Y. Zhang, Superregular breathers and state transitions in a resonant erbium-doped fiber system with higher-order effects, *Phys. Lett. A* **382**, 2650 (2018).
- [41] L. C. Zhao, S. C. Li, and L. Ling, W-shaped solitons generated from a weak modulation in the Sasa-Satsuma equation, *Phys. Rev. E* **93**, 032215 (2016).
- [42] Y. Ren, Z. Y. Yang, C. Liu, and W. L. Yang, Different types of nonlinear localized and periodic waves in an erbium-doped fiber system, *Phys. Lett. A* **379**, 2991 (2015).
- [43] L. Wang, Z. Q. Wang, J. H. Zhang, F. H. Qi, and M. Li, Stationary nonlinear waves, superposition modes and modulational instability characteristics in the AB system, *Nonlinear Dyn.* **86**, 185 (2016).
- [44] H. S. Zhang, L. Wang, X. Wang, and X. Y. Xie, Transformed nonlinear waves, state transitions and modulation instability in a three-component AB model for the geophysical flows, *Nonlinear Dyn.* **102**, 349 (2020).
- [45] H. S. Zhang, L. Wang, W. R. Sun, X. Wang, and T. Xu, Mechanisms of stationary converted waves and their complexes in the multi-component AB system, *Physica D* **419**, 132849 (2021).
- [46] X. Zhang, L. Wang, C. Liu, M. Li, and Y. C. Zhao, High-dimensional nonlinear wave transitions and their mechanisms, *Chaos* **30**, 113107 (2020).
- [47] G. Hinton, L. Deng, D. Yu, G. E. Dahl, A. R. Mohamed, N. Jaitly, A. Senior, V. Vanhoucke, P. Nguyen, T. N. Sainath *et al.*, Deep neural networks for acoustic modeling in speech recognition: The shared views of four research groups, *IEEE Signal Proc. Mag.* **29**, 82 (2012).
- [48] A. Krizhevsky, I. Sutskever, and G. E. Hinton, Imagenet classification with deep convolutional neural networks, *Commun. ACM* **60**, 84 (2017).
- [49] B. M. Lake, R. Salakhutdinov, and J. B. Tenenbaum, Human-level concept learning through probabilistic program induction, *Science* **350**, 1332 (2015).
- [50] M. Emadi, R. Taghizadeh-Mehrjardi, A. Cherati, M. Danesh, A. Mosavi, and T. Scholten, Predicting and mapping of soil organic carbon using machine learning algorithms in northern Iran, *Remote Sensing* **12**, 2234 (2020).

- [51] M. Raissi, P. Perdikaris, and G. E. Karniadakis, Physics-informed neural networks: A deep learning framework for solving forward and inverse problems involving nonlinear partial differential equations, *J. Comput. Phys.* **378**, 686 (2019).
- [52] G. F. Pang, L. Lu, and G. E. Karniadakis, fPINNs: Fractional physics-informed neural networks, *SIAM J. Sci. Comput.* **41**, A2603 (2019).
- [53] L. Yuan, Y. Q. Ni, X. Y. Deng, and S. Hao, A-PINN: Auxiliary physics informed neural networks for forward and inverse problems of nonlinear integro-differential equations, *J. Comput. Phys.* **462**, 111260 (2022).
- [54] L. Yang, D. K. Zhang, and G. E. Karniadakis, Physics-informed generative adversarial networks for stochastic differential equations, *SIAM J. Sci. Comput.* **42**, A292 (2020).
- [55] A. D. Jagtap, E. Kharazmi, and G. E. Karniadakis, Conservative physics-informed neural networks on discrete domains for conservation laws: Applications to forward and inverse problems, *Comput. Methods Appl. Mech. Eng.* **365**, 113028 (2020).
- [56] A. D. Jagtap and G. E. Karniadakis, Extended physics-informed neural networks (XPINNs) : A generalized space-time domain decomposition based deep learning framework for nonlinear partial differential equations, *Commun. Comput. Phys.* **28**, 2002 (2020).
- [57] S. Zhang, P. Lan, and J. J. Su, Wave-packet behaviors of the defocusing nonlinear Schrödinger equation based on the modified physics-informed neural networks, *Chaos* **31**, 113107 (2021).
- [58] Y. B. Zhang, L. Wang, P. Zhang, H. T. Luo, W. L. Shi, and X. Wang, The nonlinear wave solutions and parameters discovery of the Lakshmanan-Porsezian-Daniel based on deep learning, *Chaos Solitons Fractals* **159**, 112155 (2022).
- [59] J. C. Pu, W. Q. Peng, and Y. Chen, The data-driven localized wave solutions of the derivative nonlinear Schrödinger equation by using improved PINN approach, *Wave Motion* **107**, 102823 (2021).
- [60] W. Q. Peng, J. C. Pu, and Y. Chen, PINN deep learning method for the Chen–Lee–Liu equation: Rogue wave on the periodic background, *Commun Nonlinear Sci Numer Simul.* **105**, 106067 (2022).
- [61] J. C. Pu and Y. Chen, Data-driven forward-inverse problems for Yajima-Oikawa system using deep learning with parameter regularization, *Commun. Nonlinear Sci. Numer. Simul.* **118**, 107051 (2023).
- [62] L. Wang and Z. Y. Yan, Data-driven peakon and periodic peakon solutions and parameter discovery of some nonlinear dispersive equations via deep learning, *Physica D* **428**, 133037 (2021).
- [63] J. L. Wang and J. S. He, The distortion of the Peregrine soliton under the perturbation in initial condition, *Phys. Lett. A* **452**, 128432 (2022).
- [64] B. B. Kadomtsev and V. I. Petviashvili, On the stability of solitary waves in weakly dispersing media, *Sov. Phys. Dokl.* **15**, 539 (1970).
- [65] A. De Bouard and J. C. Saut, Solitary waves of generalized Kadomtsev-Petviashvili equations, *Ann. Inst. Henri Poincaré* **14**, 211 (1997).
- [66] R. S. Johnson, A two-dimensional Boussinesq equation for water waves and some of its solutions, *J. Fluid Mech.* **323**, 65 (1996).
- [67] K. Hornik, M. Stinchcombe, and H. White, Multilayer feedforward networks are universal approximators, *Neural Networks* **2**, 359 (1989).
- [68] A. G. Baydin, B. A. Pearlmutter, A. A. Radul, and J. M. Siskind, Automatic differentiation in machine learning: A survey, *J. Mach. Learn. Res.* **18**, 1 (2018).
- [69] X. Glorot and Y. Bengio, Understanding the difficulty of training deep feedforward neural networks, in *Proceedings of the 30th International Conference on Artificial Intelligence and Statistics*, 2010 (unpublished), p. 249.
- [70] D. P. Kingma and J. Ba, Adam: A method for stochastic optimization, *arXiv:1412.6980* (2014).
- [71] D. C. Liu and J. Nocedal, On the limited memory BFGS method for large scale optimization, *Math. Program.* **45**, 503 (1989).
- [72] R. Hirota, *The Direct Method in Soliton Theory* (Cambridge University, New York, 2004).
- [73] V. B. Matveev and M. A. Salle, *Darboux Transformations and Solitons* Vol. 17 (Springer, New York, 1991).
- [74] M. Stein, Large sample properties of simulations using Latin hypercube sampling, *Technometrics* **29**, 143 (1987).
- [75] Y. M. Pang, L. Wang, T. X. Liu, X. M. Yao, and S. F. Tian, Mechanisms of bright and dark transition states for the (2+1)-dimensional Boussinesq equation in shallow water (unpublished).
- [76] GitHub, <https://github.com/Liuhaiyi2000/pPINN>.